

Single-cell twitching chemotaxis in developing biofilms

Nuno M. Oliveira^{a,b,1}, Kevin R. Foster^{a,b,2}, and William M. Durham^{a,2}

^aDepartment of Zoology, University of Oxford, Oxford OX1 3PS, United Kingdom; and ^bOxford Centre for Integrative Systems Biology, University of Oxford, Oxford OX1 3PS, United Kingdom

Edited by Howard C. Berg, Harvard University, Cambridge, MA, and approved April 19, 2016 (received for review January 15, 2016)

Bacteria form surface-attached communities, known as biofilms, which are central to bacterial biology and how they affect us. Although surface-attached bacteria often experience strong chemical gradients, it remains unclear whether single cells can effectively perform chemotaxis on surfaces. Here we use microfluidic chemical gradients and massively parallel automated tracking to study the behavior of the pathogen *Pseudomonas aeruginosa* during early biofilm development. We show that individual cells can efficiently move toward chemoattractants using pili-based “twitching” motility and the Chp chemosensory system. Moreover, we discovered the behavioral mechanism underlying this surface chemotaxis: Cells reverse direction more frequently when moving away from chemoattractant sources. These corrective maneuvers are triggered rapidly, typically before a wayward cell has ventured a fraction of a micron. Our work shows that single bacteria can direct their motion with submicron precision and reveals the hidden potential for chemotaxis within bacterial biofilms.

Pseudomonas aeruginosa | bacterial chemotaxis | twitching motility | Type IV pili | Pil-Chp system

Flagella-driven chemotaxis in bacteria has been thoroughly dissected (1–4), leading to its emergence as a paradigm of both signal transduction and cellular decision-making (4, 5). However, many key phenotypes of bacteria occur when cells are not swimming. In particular, planktonic cells commonly attach to surfaces and form communities, known as biofilms, which are central to health, disease, agriculture, industry, and the environment (6, 7). Biofilms often contain steep chemical gradients that result from cell metabolism, hampered diffusion, and the secretion of a wide variety of compounds (8). Although attached bacteria can be highly motile (9–11), remarkably little is known about the potential for these cells to respond to their chemical environment.

Surface-based movement has been studied in both *Myxococcus xanthus* (12, 13) and *Pseudomonas aeruginosa* (14–16) by exposing agar-based colonies to gradients of phospholipids and unsaturated long-chain fatty acids. Over time these colonies develop a bulge toward the chemoattractant source. However, the dense packing of cells within these assays makes it difficult to resolve the cause: asymmetric colonies can form because motility is simply enhanced on the side of the colony where chemoattractants are plentiful (chemokinesis), or instead because cells are actively biasing their motility up the chemical gradient (chemotaxis) (14). Moreover, in sharp contrast to swimming bacteria, experiments with *M. xanthus* have suggested that solitary surface-attached bacteria are incapable of biasing their motility along chemical gradients (13, 17). We, therefore, designed a new assay to test whether individual cells can perform chemotaxis on surfaces (*SI Appendix, SI Materials and Methods*). Our experiments reveal that not only are single cells capable of chemotaxis, but they can control their position with a striking level of precision.

Results and Discussion

Individual Bacteria Can Navigate Chemical Gradients on Surfaces. *P. aeruginosa* is an intensely studied opportunistic pathogen and a canonical model for the study of biofilms (18). After attaching to surfaces, *P. aeruginosa* cells are highly motile and move by pulling themselves along via the extension and retraction of their type IV pili, a process known as twitching motility (19). Although

this form of movement is common throughout biofilm formation (10, 11), here we follow the movement of solitary bacteria in the early stages of biofilm development so that we can readily calculate each cell's chemical environment and resolve how it modifies their behavior. Importantly, the microfluidic assays used here are analogous to those used in classical studies of biofilm development (9–11), and the cells whose movement we analyze subsequently form 3D biofilm structures (Fig. 1 *F* and *G* and *SI Appendix, Fig. S1*). To generate stable chemical gradients, we use two inlet microfluidic devices where flow balances the smoothing effect of molecular diffusion (Fig. 1*A* and *SI Appendix, Fig. S2* and *SI Materials and Methods*). Many bacterial chemoattractants strongly promote growth (20), which in our experiments leads to a crowded surface and a limited ability to analyze single cell behavior. We therefore began our experiments with DMSO, which is a known chemoeffector of bacteria (21–23) and, importantly, does not strongly affect growth in our experiments.

We used automated cell tracking to follow surface-attached *P. aeruginosa* cells that are exposed to a stable spatial gradient of DMSO (Fig. 1*A* and *SI Appendix, Fig. S2*). Our method allows us to follow large numbers of attached cells and quantify their individual responses to the presence, or absence, of a chemical gradient (*SI Appendix, Fig. S3*). In a DMSO gradient, we found that cell movement is strongly biased in the direction of increasing DMSO concentration (Fig. 1*B* and *Movie S1*), which contrasted with random motility in the absence of chemical gradients (Fig. 1*C* and *D*). After 2 h of incubation, the chemotactic bias peaks, with more than three times as many cells moving toward the chemoattractant source than moving away from it ($\beta = 3.1$), but biased motility is maintained even as the surface becomes more crowded with cells (Fig. 1*D* and *E*). These data show single cells direct their motility along chemical gradients and suggest that surface-attached cells are capable of chemotaxis [*sensu* Adler (1)].

Significance

Bacterial biofilms affect many aspects of our lives, from causing disease to promoting health and shaping many key processes in the environment. Despite this, surface-attached cells in biofilms are often portrayed as static and sluggish, a stark contrast to the energetic swimming they exhibit in liquid. Here we use microfluidic devices and automated cell tracking to challenge this view: We find that individual cells will actively move toward nutrients within a developing biofilm. This ability not only allows cells to seek out favored positions on a surface but our analyses show that they can regulate their movement with remarkable submicron precision. Our findings suggest we can systematically engineer biofilms by manipulating the movement of the cells from which they are founded.

Author contributions: N.M.O., K.R.F., and W.M.D. designed research; N.M.O. and W.M.D. performed research; N.M.O. and W.M.D. analyzed data; and N.M.O., K.R.F., and W.M.D. wrote the paper.

The authors declare no conflict of interest.

This article is a PNAS Direct Submission.

¹Present address: Cell Biology Division, Medical Research Council Laboratory of Molecular Biology, Cambridge Biomedical Campus, Cambridge CB2 0QH, United Kingdom.

²To whom correspondence may be addressed. Email: kevin.foster@zoo.ox.ac.uk or william.durham@zoo.ox.ac.uk.

This article contains supporting information online at www.pnas.org/lookup/suppl/doi:10.1073/pnas.1600760113/-DCSupplemental.

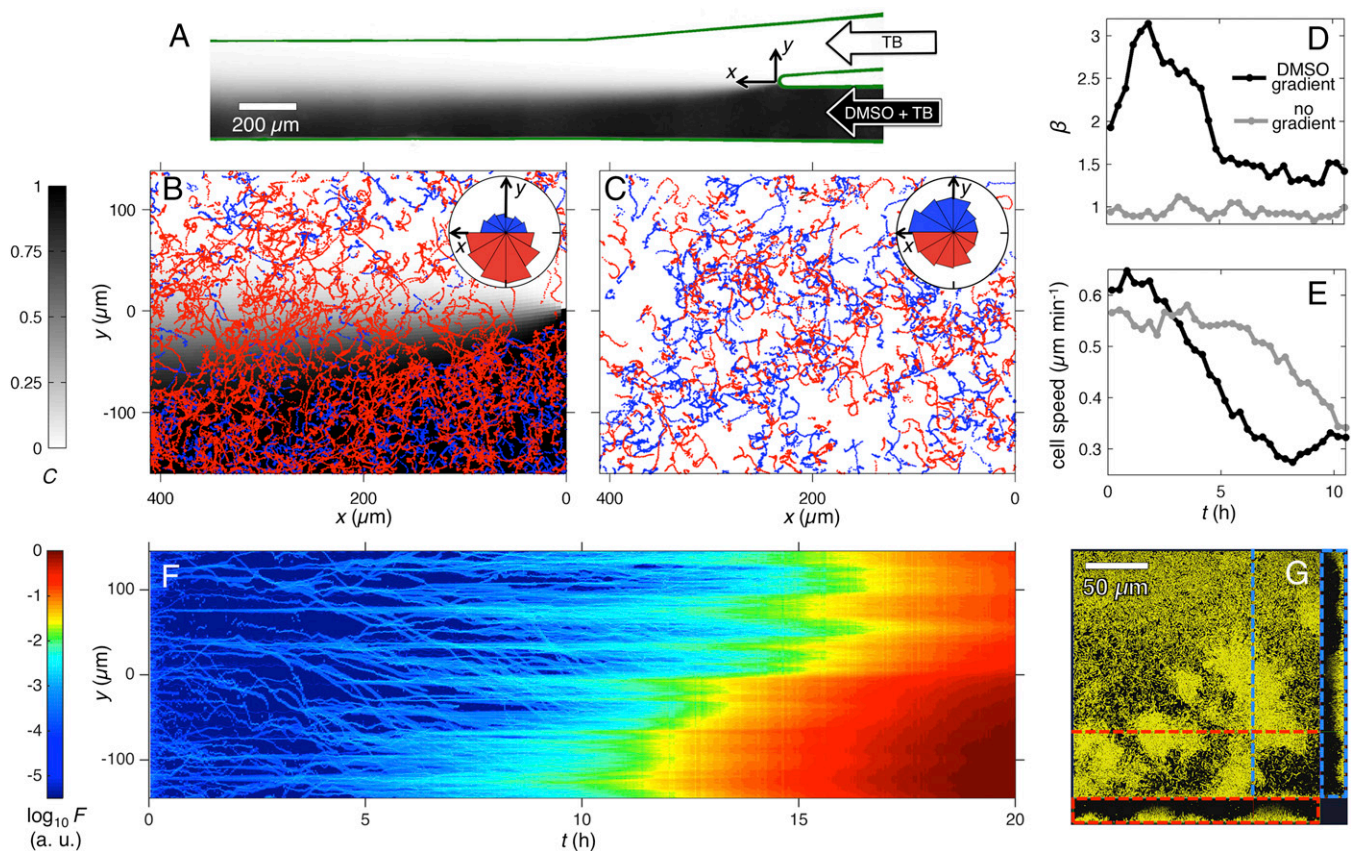


Fig. 1. Surface-attached *P. aeruginosa* cells direct their movement up gradients of DMSO during biofilm formation. (A) A two-inlet microfluidic device generates a stable chemical gradient via molecular diffusion. TB is continuously injected through one of the inlets, whereas DMSO at a concentration of $C_{\text{MAX}} = 350$ mM and TB are continuously injected through the other inlet. Here $C = C/C_{\text{MAX}}$, where C is the local concentration of DMSO that was quantified using fluorescein in a separate experiment (SI Appendix, Fig. S2 and SI Materials and Methods). (B) Cell trajectories over the first 5 h of the experiment ($t = 0$ –5 h) show that motility is biased toward increasing concentrations of DMSO. Trajectories with net movement toward larger C (i.e., in $-y$) are shown in red and those with net movement toward smaller C (i.e., in $+y$) are shown in blue. The background shows C computed by a mathematical model (SI Appendix, Fig. S2). Inset shows probability density functions of the angle from each trajectory's origin to final position and red (blue) bins denote movement in the $-y$ ($+y$) direction (SI Appendix, SI Materials and Methods). This Inset also shows slight preferential movement in the $+x$ direction, which likely results from interactions with flow (39). (C) Control shows there is no bias in the y direction without DMSO. (D and E) A time series of the chemotactic bias, β , defined as the number of cells that move in $-y$ divided by the number moving in $+y$, peaks at $t \approx 2$ h (D; black line; gray line shows control) and then declines as the surface becomes more crowded and cell speed is attenuated (E). (F) A kymograph of the fluorescent intensity, F , of cells that constitutively produce yellow fluorescent protein (SI Appendix, SI Materials and Methods) show how biofilms develop over time in our experiments. Here we average the fluorescent intensity in x , allowing us to continuously resolve both the chemotaxis of cells (light blue streaks moving toward $-y$) and formation of densely packed biofilms (red). As biofilms produce a much brighter fluorescent signal than single cells we plot the logarithm of F so that both can be visualized. SI Appendix, Fig. S1 shows the raw images from which this kymograph was constructed. (G) A 3D confocal micrograph of the biofilm shown in F, imaged at $t = 20$ h, shows the biofilm is already many cells thick, extending ≈ 20 μm from the surface. Dashed lines indicate the positions of the vertical cross sections.

In our experiments, both cell division and motility cause cells to preferentially accumulate on the side of the device with the chemoattractant (Fig. 1F and Movie S1). To test whether the biased motility we observe is an artifact of the variation in cell density, which has been shown coordinate surface motility in *M. xanthus* (24), we exposed cells to a chemoattractant gradient that switched direction every 3 h. By minimizing crowding on one side of the channel, this assay also allows us to study the responses of individual cells to nutrients like succinate, which is a preferred carbon source of *P. aeruginosa* and a potent chemoattractant of cells in the planktonic state (25). When the chemoattractant gradient was inverted, cells responded by changing the direction of their bias to track the gradient (Fig. 2A–G). The refinement with which individual cells dynamically track the gradient can be observed in Movie S2. Our data show that cells are directly responding to the imposed gradient rather than to de novo gradients generated by the cells. Moreover, we observe these responses for gradients of both DMSO and succinate, the latter of which strongly stimulates both growth and cell motility (SI Appendix, Fig. S4). Finally, the increased data available from this second assay reveals that the chemotactic

bias, β , increases with the magnitude of the chemoattractant $|G|$ (Fig. 2H), which is a defining feature of chemotaxis across different biological systems (26). Based on the responses seen in our two single-cell assays (Figs. 1 and 2), we conclude that individual surface-attached bacteria are indeed capable of chemotaxis.

Attached *P. aeruginosa* Use Pili-Based Motility and the Chp Chemotaxis System to Perform Chemotaxis. What is the genetic basis of the chemotactic response we documented above? After attachment, *P. aeruginosa* is well known to use pili-based motility to move on surfaces (9–11, 18, 19). Accordingly, a mutant that cannot generate functional pili (ΔpilB) is immobile in our experiments (Fig. 3A and C), whereas a mutant that lacks flagella (ΔflgK) exhibits surface motility (SI Appendix, Fig. S5). We find flagella mutant cells stand upright and show increased motility relative to WT, which is in agreement with a previous study (27), and suggests that flagella may function as a stabilizing anchor during twitching motility. To explore if the flagella could play a role in chemotaxis, we studied the behavior of mutant that has a flagellum but lacks the ability to perform flagella-based chemotaxis. Chemotaxis in swimming

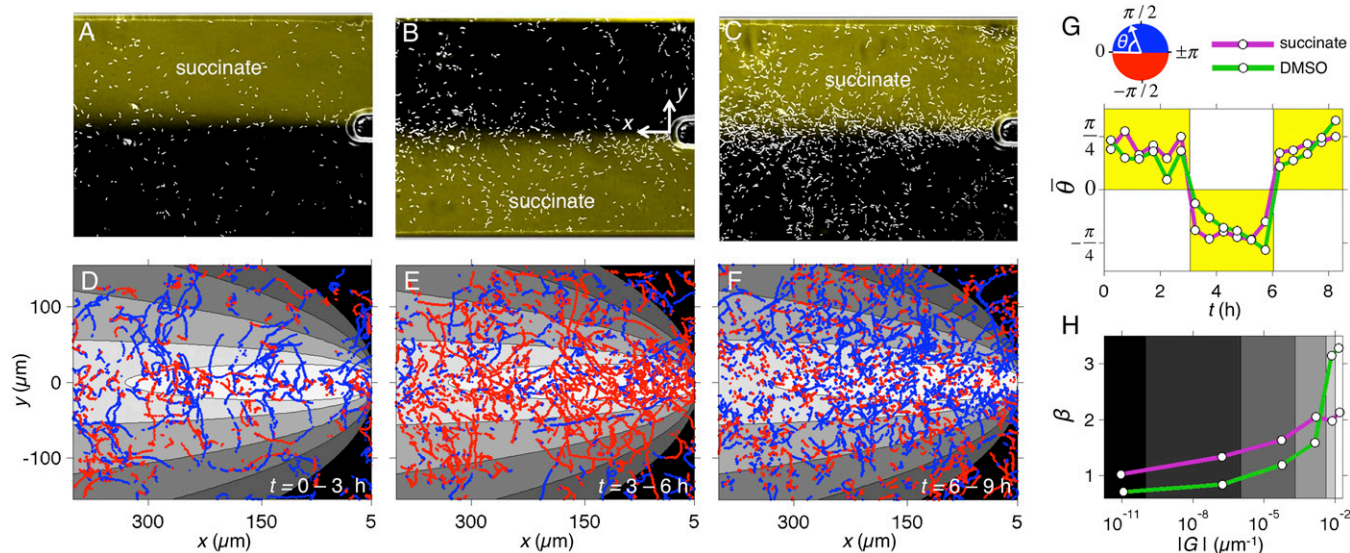


Fig. 2. Changing the direction of the chemoattractant gradient elicits a change in the direction of cell motility and reveals the chemotactic response increases with the strength of the gradient. (A–C) Cells (white spots) were exposed to gradient of succinate (visualized in yellow, $C_{\text{MAX}} = 2$ mM) whose direction was inverted every 3 h. (D–F) The resulting chemotactic response was measured by calculating the direction of cell movement, θ , over 16-min intervals, and segments of trajectories that moved in the $-y$ ($+y$) direction are shown in red (blue). (G) The mean movement direction, $\bar{\theta}$, was obtained by averaging θ for all cells (magenta line), revealing that cell motility is maintained in the direction of the instantaneous chemoattractant gradient (yellow regions). (H) Combining data from the entire experiment ($t = 0$ –9 h) reveals that the chemotactic bias, β , increases with the magnitude of the normalized gradient, $|G| = 1/C_{\text{MAX}} |\partial C/\partial y|$ (magenta line). Here β is the number of trajectories moving in the direction of increasing concentration C , divided by the number moving in the direction of decreasing C . Grayscale colors in D–F show $|G|$ and correspond to the bins used in the analysis presented in H. Green lines in G and H show results of an analogous experiment conducted with a DMSO gradient ($C_{\text{MAX}} = 350$ mM). In both experiments, the position of chemoattractant was visualized using a dye that does not induce a chemotactic response (SI Appendix, Fig. S15), and $|G|$ was estimated using a mathematical model of diffusion (SI Appendix, SI Materials and Methods).

P. aeruginosa cells is under the regulation of a Che transduction system homologous to that of *Escherichia coli* (16, 28), and mutants in CheY1, the key response regulator, can swim but cannot actively bias their movement along chemical gradients. In contrast to swimming, however, we find that the swimming chemotaxis cluster (Che cluster I) is not required for chemotaxis on surfaces because CheY1 mutants perform twitching chemotaxis (SI Appendix, Fig. S6).

Recent work has shown that twitching motility in *P. aeruginosa* is under the regulation of a separate signal-transduction pathway (Che cluster IV) known as the Chp system (16, 29) (Fig. 3B), but to date, there is no direct evidence that this system plays an active role in any form of chemotaxis. To examine the effects of the Chp system, we first recapitulated the motility phenotypes recently described using classical agar-based assays (29). Specifically, in-frame deletion mutants $\Delta pilB$, $\Delta chpA$, and $\Delta pilG$ do not form the characteristic twitching rings at the plastic–agar interface around colonies, whereas $\Delta pilH$ cells exhibit an intermediate phenotype by producing rings that are smaller than that of the WT (SI Appendix, Fig. S7). However, observing the movement of individual cells in our microfluidic system reveals a very different pattern. We find that $\Delta chpA$ and $\Delta pilG$ cells, which were previously diagnosed as incapable of twitching (29), are in fact both motile (Fig. 3A and C). While $\Delta pilH$ cells show reduced twitching rings on agar plates (SI Appendix, Fig. S7), in our microfluidic assays they actually move ≈ 30 times faster than the WT (Fig. 3A and C) and tend to orient themselves vertically on the surface (SI Appendix, Fig. S8). More formally, the root mean squared displacement (RMSD), a combined measure of both movement speed and the persistence in movement direction (30), of the WT and $\Delta pilG$ cells are nearly identical, but show strong differences with that from $\Delta chpA$ and $\Delta pilH$ (Fig. 3C).

The Chp system then has strong effects on twitching motility in our assay but is it involved in chemotaxis? To answer this question, we focused on the response regulator of the Chp system PilG, which controls pili extension (29). We focused on PilG because the motility of $\Delta pilG$ is similar to the WT in our microfluidic assay, and we can study the effects on chemotaxis in the absence of strong

effects on motility (Fig. 3A and C and Movies S3 and S4). We exposed $\Delta pilG$ cells to a stable DMSO gradient and used our analysis pipeline to track individual cells. The data reveal that, although $\Delta pilG$ cells indeed remain motile, they lack the ability to bias their motion up the gradient (Fig. 3D and E). Our results then suggest that the Chp system is not just involved in the biosynthesis of type IV pili but also in the transduction of chemotactic stimuli into directed movement.

P. aeruginosa Uses a "Pessimistic" Chemotactic Strategy on Surfaces.

We next sought to understand how *P. aeruginosa* cells bias their movement on surfaces. Chemotaxis in swimming *E. coli* cells is achieved by cells performing straight runs interspersed by sharp reorientations (tumbles), where tumbles are delayed when moving up a chemoattractant gradient (2, 3). Do twitching bacteria use similar movement strategies in our experiments? Although twitching motility gets its name from the jerky motion that cells exhibit over the timescale of minutes (31), we find that in chemical gradients cells can maintain a consistent movement direction for periods longer than 1 h (Fig. 4A). Moreover, these twitching runs are interspersed by events where a cell reverses by stopping and then moving back in the opposite direction without turning. Twitching *P. aeruginosa* cells pull themselves along surfaces with pili that cluster at their poles (32, 33), which drives movement parallel to their long axis (SI Appendix, Fig. S9) and allows rapid changes in direction if a cell changes the pole that it is pulling from. To follow this process, we developed an automated algorithm that detects when the cell's movement switches direction such that a cell's leading pole becomes its trailing pole. Importantly, we distinguish these active reversals from changes in direction that occur passively due to cell division (Fig. 4A and B, Movies S3 and S4, and SI Appendix, SI Materials and Methods).

Both $\Delta pilG$ and WT cells were found to actively reverse their direction in both the presence and absence of DMSO gradients. However, $\Delta pilG$ cells, which do not show chemotaxis (Fig. 3D and E), reversed at a much lower rate than WT cells in both of these conditions, suggesting that the reversals are indeed important for chemotaxis (Fig. 4C). To examine the potential link

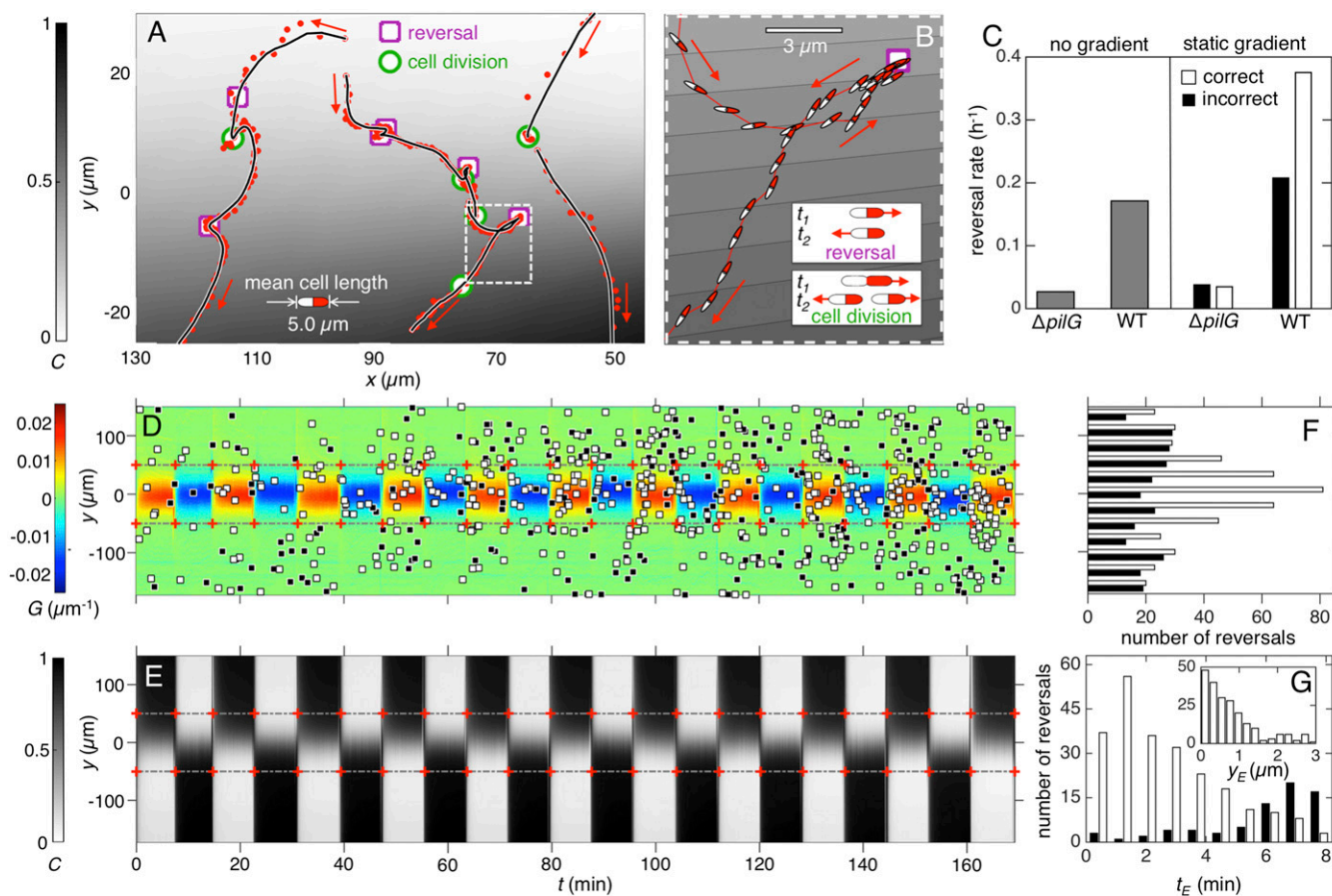


Fig. 4. Twitching bacteria chemotax by reversing their motility when traveling away from the chemoattractant source. (A) Cells navigate up DMSO gradients by actively performing reversals (magenta squares), although sharp changes in direction can also occur passively during cell division (green circles). Red dots in A show positions of cell centroids at 1-min intervals; the black lines show smoothed trajectories, and the average cell length is shown for reference. (B) Magnified view of a reversal shows a cell whose movement begins to veer toward decreasing C . The cell quickly performs a reversal sending it back up the DMSO gradient. Ellipses (not drawn to scale) show cell orientation and position in 2-min intervals. Contours show modeled DMSO concentration in $C_{\text{MAX}}/30$ increments where $C_{\text{MAX}} = 350$ mM. (C) In both the absence and presence of a DMSO gradient $\Delta pilG$ cells actively reverse at a much smaller rate than WT cells. For experiments with a DMSO gradient, we calculated the frequency that cells moving toward smaller C reverse direction (labeled correct, white bars) and the frequency that cells moving toward larger C reverse direction (labeled incorrect, black bars). Although the rate of incorrect reversals in the WT is similar to that in the absence of a gradient (gray bar), correct reversals occur more frequently, suggesting that reversals are deployed as a corrective strategy. (D–G) Using a custom microfluidic device (SI Appendix, Fig. S11), we induced reversals by exposing cells to a DMSO gradient that changed direction every eight minutes. Owing to a large flow velocity, C and its gradient $G = 1/C_{\text{MAX}} \partial C/\partial y$ were nearly constant along our field of view, allowing us to average them along x and present their spatiotemporal variations using kymographs (D and E) (SI Appendix, SI Materials and Methods). Cell reversals were identified using an automated algorithm and classified as correct (white squares, D) or incorrect (black squares, D). Both types of reversals increased over time as cell division and attachment increased the number of cells on the surface (D). Counting the number of correct and incorrect reversals within equally spaced bins in y reveals that correct reversals (white bars, F) peak along the middle of the device, whereas the number of incorrect reversals (black bars, F) occurs more uniformly in y . The reaction time, t_E , is the time elapsed from the most recent gradient change (red + symbols in E and F) to the time of a correct reversal. A histogram of t_E for cells in middle 100 μm of the device (dashed gray lines; D and E) shows that correct reversals peak ≈ 1 min after the gradient changes direction (G). Over this period most cells travel a distance along the gradient, y_E , less than 1 μm (G, Inset).

that changes direction every eight minutes (Fig. 4 D and E and SI Appendix, Fig. S11). Direct observation suggests that twitching *P. aeruginosa* cells accurately reverse their movement in response to the alternating gradient (Movie S5), and we quantified their response by categorizing all reversal events as correct or incorrect. Correct reversals occurred in cells moving away from the chemoattractant source and incorrect reversals occurred in cells moving toward the source (Fig. 4 D and E and Movie S6). We find that correct reversals are stimulated by the alternating gradient (rather than incorrect reversals being repressed), which is again consistent with a pessimistic chemotactic response (Fig. 4F). In addition, we find that WT cells actively increase their speed after performing correct reversals but not after performing incorrect reversals (SI Appendix, Fig. S12). In contrast, cells lacking PilG reversed very rarely in the alternating chemical gradient (SI Appendix, Fig. S13). Taken together, these observations show that attached *P. aeruginosa*

chemotax by deploying reversals when their motility is directed away from the source of a chemoattractant. Correct reversals occurred most frequently in the middle of the device, where cells are exposed to the strongest spatial gradients in DMSO (Fig. 4 D and F) and these reversals peak $t_E \approx 1$ min after the gradient changes direction (Fig. 4G). The rapid response means that the majority of cells sense the gradient has changed direction and respond before moving one-fifth the length of their bodies (SI Appendix, Fig. S14), a distance smaller than a micrometer (Fig. 4G, Inset). This observation reveals that attached *P. aeruginosa* can regulate their movement in a chemical gradient with submicron precision.

Swimming bacteria sense chemoattractant gradients by measuring changes in chemical concentrations over time, which is consistent with them moving rapidly and thus being able to detect large changes over short time periods (2, 34). However, the slow speed and highly unsteady, oscillatory movement of twitching cells (31) begs the

question of whether they too use temporal sensing. If twitching cells do use temporal sensing, it would require the integration of information over much longer time-scales than swimming bacteria. Moreover, a twitching cell would have to extract the slow, weak changes in concentration due to their average movement from the large, high-frequency changes in concentration that arise from a cell jerking back and forth relative to a chemical gradient. An intriguing alternative is that twitching cells detect gradients spatially by directly measuring changes in concentration across the length of their bodies. Indeed, in our experiments (Fig. 4 D–G), the majority of responding cells experience a fivefold larger change in chemoattractant concentration across their length than they experience over time due to their movement relative to the gradient (SI Appendix, Fig. S14). Although the fast movement of swimming cells allow them to measure changes in concentration over distances equivalent to tens of their body lengths (2), the slow movement of twitching cells suggests that they could collect more reliable information by making spatial measurements, over the length of their body. In either case, our data suggest that the molecular mechanisms underlying twitching chemotaxis have very different properties than the canonical mechanisms so intensively studied in swimming cells.

Conclusion

Bacteria often live attached to surfaces where multiple strains and species meet and interact (35). These cells strongly alter their environment by secreting a wide range of compounds and metabolizing others to create a diverse and changing set of chemical gradients (8). The resulting chemical gradients can be very steep, stable, and important for the fitness of cells that lie in different positions within a community (36). Here we showed that single attached bacteria can respond to chemical gradients. Rather like ants moving through a nest, we find that twitching cells are able to act as individuals that navigate their way through their chemical

and biological environment. We also show that these surface-attached cells perform chemotaxis on spatial scales much finer than swimming cells, with corrective maneuvers occurring before a cell has moved a small fraction of their body length. The discovery that bacteria can navigate their chemical environment with sub-micron precision has implications for both the biology of bacterial communities and how we manipulate them.

Materials and Methods

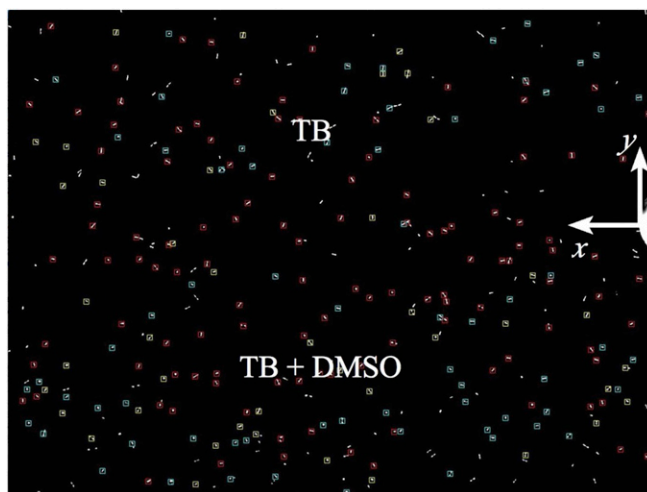
Our experiments use WT *P. aeruginosa* PAO1 (Kolter collection, ZK2019) as a working model for twitching chemotaxis (Figs. 1 and 2 and SI Appendix, Figs. S3, S9, and S15). The YFP-labeled strain used in Fig. 1 F and G and SI Appendix, Fig. S1 is a PAO1 WT strain with a ZK2019 background (37). Δ flgK (SI Appendix, Fig. S5), which has been published and described before (38), is a deletion strain lacking the hook filament junction protein FlgK. To study the functional role of the Chp chemosensory system, we used in-frame deletion mutants of *pilB*, *chpA*, *pilG*, and *pilH*, along their respective WT, which have all been published and described elsewhere (29). These strains are used in Figs. 3 and 4 and SI Appendix, Figs. S4, S7, S8, S10, S12–S14, and S16. The Δ cheY1 mutant strain shown in SI Appendix, Fig. S6 was a gift from the group of Caroline Harwood, University of Washington, Seattle. All strains were grown in shaken culture overnight in LB (37 °C) from frozen stocks and subcultured to obtain cells in exponential phase. These were then diluted to an optical density of 0.25 (at 600 nm) in tryptone broth (TB; 10 g Bacto tryptone/1 L water) before they were injected into our microfluidic devices.

ACKNOWLEDGMENTS. We thank Joanne Engel for the Pii-Chp mutants, Caroline Harwood for the CheY1 mutant, Jean-Yves Tinevez for help with the Trackmate code, and Michael Laub for discussions. Judith Armitage, Howard Berg, Eamonn Gaffney, Jeffery Guasto, Michael Laub, Timothy Pedley, Roman Stocker, and Gerard Wong provided comments on preliminary versions of this manuscript. This work was funded by a Fundação para a Ciência e Tecnologia Studentship SFRH-BD-73470-2010 (to N.M.O.), European Research Council Grant 242670 (to K.R.F.), and a Human Frontier Science Program Fellowship LT001181/2011L (to W.M.D.).

- Adler J (1966) Chemotaxis in bacteria. *Science* 153(3737):708–716.
- Berg HC (2004) *E. coli in Motion* (Springer, New York).
- Berg HC, Brown DA (1972) Chemotaxis in *Escherichia coli* analysed by three-dimensional tracking. *Nature* 239(5374):500–504.
- Wadhams GH, Armitage JP (2004) Making sense of it all: Bacterial chemotaxis. *Nat Rev Mol Cell Biol* 5(12):1024–1037.
- Porter SL, Wadhams GH, Armitage JP (2011) Signal processing in complex chemotaxis pathways. *Nat Rev Microbiol* 9(3):153–165.
- Costerton JW, Lewandowski Z, Caldwell DE, Korber DR, Lappin-Scott HM (1995) Microbial biofilms. *Annu Rev Microbiol* 49:711–745.
- Kolter R, Greenberg EP (2006) Microbial sciences: The superficial life of microbes. *Nature* 441(7091):300–302.
- Stewart PS, Franklin MJ (2008) Physiological heterogeneity in biofilms. *Nat Rev Microbiol* 6(3):199–210.
- Klausen M, Aaes-Jørgensen A, Molin S, Tolker-Nielsen T (2003) Involvement of bacterial migration in the development of complex multicellular structures in *Pseudomonas aeruginosa* biofilms. *Mol Microbiol* 50(1):61–68.
- Klausen M, et al. (2003) Biofilm formation by *Pseudomonas aeruginosa* wild type, flagella and type IV pili mutants. *Mol Microbiol* 48(6):1511–1524.
- Zhao K, et al. (2013) Psl trails guide exploration and microcolony formation in *Pseudomonas aeruginosa* biofilms. *Nature* 497(7449):388–391.
- Shi W, Köhler T, Zusman DR (1993) Chemotaxis plays a role in the social behaviour of *Myxococcus xanthus*. *Mol Microbiol* 9(3):601–611.
- Zhang Y, Ducret A, Shaevitz J, Mignot T (2012) From individual cell motility to collective behaviors: Insights from a prokaryote, *Myxococcus xanthus*. *FEMS Microbiol Rev* 36(1):149–164.
- Kearns DB, Robinson J, Shimkets LJ (2001) *Pseudomonas aeruginosa* exhibits directed twitching motility up phosphatidylethanolamine gradients. *J Bacteriol* 183(2):763–767.
- Miller RM, et al. (2008) *Pseudomonas aeruginosa* twitching motility-mediated chemotaxis towards phospholipids and fatty acids: Specificity and metabolic requirements. *J Bacteriol* 190(11):4038–4049.
- Sampedro I, Parales RE, Krell T, Hill JE (2015) *Pseudomonas* chemotaxis. *FEMS Microbiol Rev* 39(1):17–46.
- Taylor RG, Welch RD (2008) Chemotaxis as an emergent property of a swarm. *J Bacteriol* 190(20):6811–6816.
- O'Toole GA, Kolter R (1998) Flagellar and twitching motility are necessary for *Pseudomonas aeruginosa* biofilm development. *Mol Microbiol* 30(2):295–304.
- Burrows LL (2012) *Pseudomonas aeruginosa* twitching motility: Type IV pili in action. *Annu Rev Microbiol* 66(6):493–520.
- Adler J, Hazelbauer GL, Dahl MM (1973) Chemotaxis toward sugars in *Escherichia coli*. *J Bacteriol* 115(3):824–847.
- Shi W, Köhler T, Zusman DR (1994) Isolation and phenotypic characterization of *Myxococcus xanthus* mutants which are defective in sensing negative stimuli. *J Bacteriol* 176(3):696–701.
- Seymour JR, Simó R, Ahmed T, Stocker R (2010) Chemoattraction to dimethylsulfoniopropionate throughout the marine microbial food web. *Science* 329(5989):342–345.
- Packer HL, Gauden DE, Armitage JP (1996) The behavioural response of anaerobic *Rhodobacter sphaeroides* to temporal stimuli. *Microbiology* 142(Pt 3):593–599.
- Kaiser D (2003) Coupling cell movement to multicellular development in myxobacteria. *Nat Rev Microbiol* 1(1):45–54.
- Moulton RC, Montie TC (1979) Chemotaxis by *Pseudomonas aeruginosa*. *J Bacteriol* 137(1):274–280.
- Rivero MA, Tranquillo RT, Buettner HM, Lauffenburger DA (1989) Transport models for chemotactic cell populations based on individual cell behavior. *Chem Eng Sci* 44(12):2881–2897.
- Conrad JC, et al. (2011) Flagella and pili-mediated near-surface single-cell motility mechanisms in *P. aeruginosa*. *Biophys J* 100(7):1608–1616.
- Kato J, Kim HE, Takiguchi N, Kuroda A, Ohtake H (2008) *Pseudomonas aeruginosa* as a model microorganism for investigation of chemotactic behaviors in ecosystem. *J Biosci Bioeng* 106(1):1–7.
- Bertrand JJ, West JT, Engel JN (2010) Genetic analysis of the regulation of type IV pilus function by the Chp chemosensory system of *Pseudomonas aeruginosa*. *J Bacteriol* 192(4):994–1010.
- Gibiński ML, et al. (2010) Bacteria use type IV pili to walk upright and detach from surfaces. *Science* 330(6001):197.
- Jin F, Conrad JC, Gibiński ML, Wong GCL (2011) Bacteria use type-IV pili to slingshot on surfaces. *Proc Natl Acad Sci USA* 108(31):12617–12622.
- Cowles KN, Gitai Z (2010) Surface association and the MreB cytoskeleton regulate pilus production, localization and function in *Pseudomonas aeruginosa*. *Mol Microbiol* 76(6):1411–1426.
- Skerker JM, Berg HC (2001) Direct observation of extension and retraction of type IV pili. *Proc Natl Acad Sci USA* 98(12):6901–6904.
- Segall JE, Block SM, Berg HC (1986) Temporal comparisons in bacterial chemotaxis. *Proc Natl Acad Sci USA* 83(23):8987–8991.
- Nadell CD, Xavier JB, Foster KR (2009) The sociobiology of biofilms. *FEMS Microbiol Rev* 33(1):206–224.
- Kim W, Racimo F, Schluter J, Levy SB, Foster KR (2014) Importance of positioning for microbial evolution. *Proc Natl Acad Sci USA* 111(16):E1639–E1647.
- Oliveira NM, et al. (2015) Biofilm formation as a response to ecological competition. *PLoS Biol* 13(7):e1002191.
- Caldara M, et al. (2012) Mucin biopolymers prevent bacterial aggregation by retaining cells in the free-swimming state. *Curr Biol* 22(24):2325–2330.
- Shen Y, Siryaporn A, Lecuyer S, Gitai Z, Stone HA (2012) Flow directs surface-attached bacteria to twitch upstream. *Biophys J* 103(1):146–151.

Supporting Information

Oliveira et al. 10.1073/pnas.1600760113



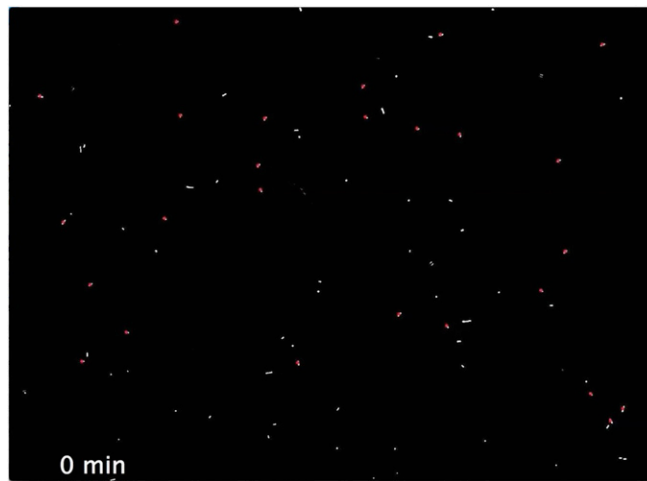
Movie S1. Surface-attached cells display chemotaxis in a static gradient of DMSO. Cells with red trajectories are traveling toward higher concentrations of DMSO, cells with cyan trajectories are traveling toward lower concentrations of DMSO, and cells with yellow trajectories display little net movement in any direction. The latter are distinguished by measurements of the net to gross displacement ratio (NGDR < 0.15; *SI Appendix, SI Materials and Methods*).

[Movie S1](#)



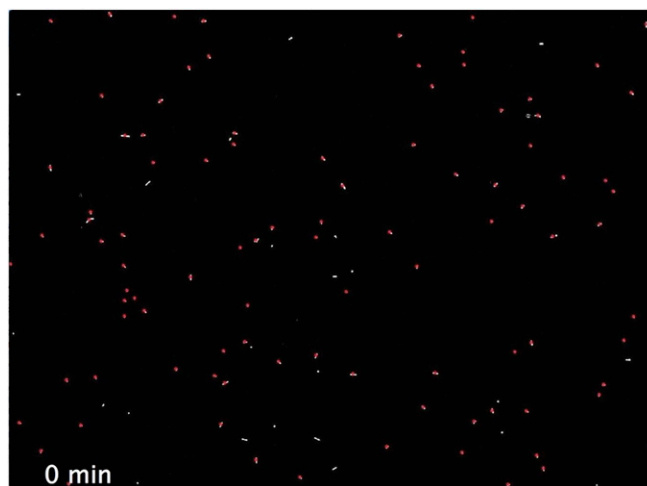
Movie S2. Surface-attached cells bias their motility to track gradients of succinate. Dye is used to visualize the distribution of succinate (*SI Appendix, SI Materials and Methods*), which here has been processed to appear yellow. We alternate the direction of the gradient every 3 h, and cells respond by biasing their movement such that they consistently move toward larger concentrations of succinate.

[Movie S2](#)



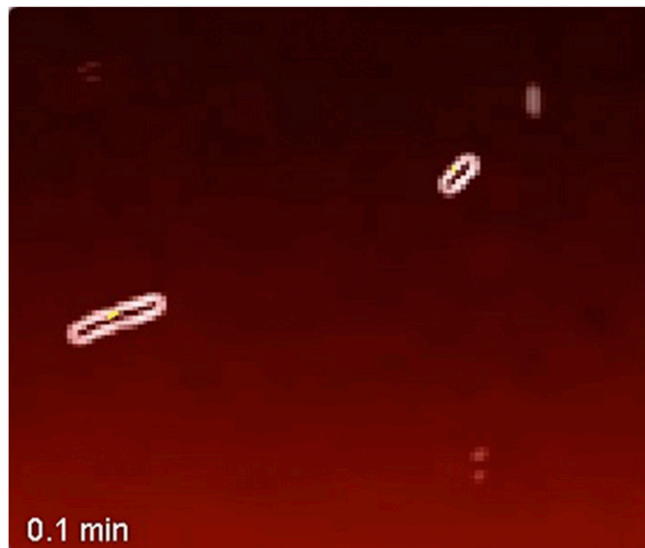
Movie S3. WT cells perform reversals in the absence of chemical gradients. By definition, a reversal occurs when a cell stops and moves back in the other direction without turning. Reversals can be observed when a cell's leading pole, the end of the cell that is pointing in the direction of movement (small green circles), shifts to the opposite side of the cell. Cells performing true reversals are marked with yellow rings, reversals associated with cell division are marked with cyan rings, and reversals that occur too close to the end of the trajectories to ascertain their origin are shown with magenta rings (*SI Appendix, SI Materials and Methods*). Cells whose motility is being actively monitored for reversals are marked with a small red dot.

[Movie S3](#)



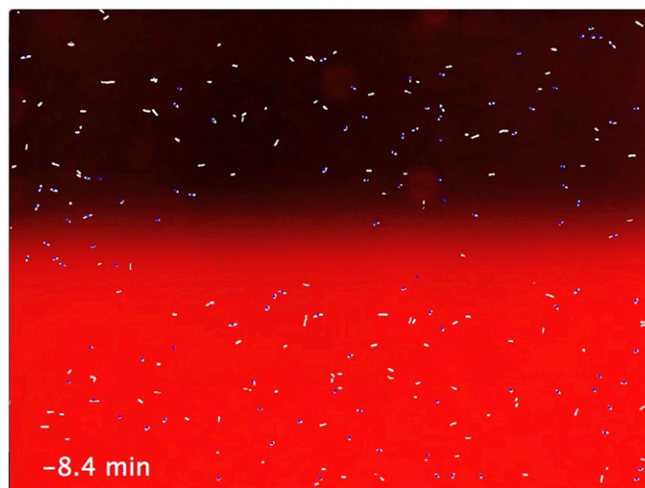
Movie S4. Cells lacking the response regulator PilG, homolog of CheY of *E. coli*, reverse less frequently than WT cells. Here we analyze the movement of $\Delta pilG$ cells that are exposed to the same conditions as shown in Movie S3, and we use the same notation to mark the reversals. Compared with the WT, $\Delta pilG$ cells perform true reversals (thick yellow rings) less frequently (Fig. 4C).

[Movie S4](#)



Movie S5. Cells reverse to track a DMSO gradient that rapidly changes direction. We visualized the DMSO gradient, which changes direction every 8 min, using dye (shown here in red; *SI Appendix, SI Materials and Methods*). The two cells highlighted here reverse direction to keep their motility directed toward larger concentrations of DMSO. All reversals are marked with yellow rings and the leading poles of cells are denoted with small green circles. Yellow lines show cell trajectories.

[Movie S5](#)



Movie S6. Cells exposed to a rapidly alternating DMSO gradient reverse most frequently in the middle of the device, where spatial gradients of chemo-attractant are the largest. Dye is used to visualize the instantaneous distribution of DMSO, which here has been processed to appear red. Correct reversals (white rings) occur in cells whose leading pole (small green circles) is initially directed down the DMSO gradient, whereas incorrect reversals (light blue rings) occur in cells whose leading pole is initially directed up the DMSO gradient. Cells whose motility is being actively monitored for reversals are marked with a small blue circle.

[Movie S6](#)

Other Supporting Information Files

[SI Appendix \(PDF\)](#)

Single-cell twitching chemotaxis in developing biofilms

Supplementary Information

We present below a detailed description of our microfluidic experiments and quantitative analyses, in addition to our 16 supplementary figures.

Materials and Methods

Subsurface twitching assay

We followed standard protocols previously described (1, 2). Briefly, strains were grown in shaken culture overnight in LB (37°C), spotted on 1.5% LB agar, and then incubated at 37°C for 24 hours. These cells were used to stab-inoculate Petri dishes filled with 1% agar (LB or TB) to deposit bacteria at the interface between the agar and the underlying plastic dish. After 48 hours of incubation at 37°C the dishes were photographed with a DSLR camera (EOS 30D, Canon). The software Fiji (3) was used to enhance the contrast (over the whole image) to make the relatively faint twitching rings on the bottom of the plate more visible.

Microfluidic experiments

Two different microfluidic setups were used in this study. We used the commercially available Bioflux 200 system (Fluxion Biosciences) for all microfluidic experiments except the alternating gradient experiments presented in Fig. 4D-G and Figs. S12, S13, S14, which used a custom designed microfluidic device (Fig. S11). Briefly,

microfluidic channels were primed with tryptone broth (TB) medium as previously described (4). Exponential phase cells were then introduced at an OD of 0.25 and allowed to attach to the surface for 20 min in the absence of flow. Planktonic and weakly adhered cells were then flushed from the test section by applying a flow rate of $40 \mu\text{l h}^{-1}$ for 10 min. The flow rate was then reduced to $4 \mu\text{l h}^{-1}$ at $t = 0$, which was maintained for the remainder of the experiment. Cells were imaged at a rate of 1 frame min^{-1} , with the exception of the $\Delta pilH$ (Fig. 3) and $\Delta flgK$ mutants (Fig. S5), which, due to their very fast motility, were imaged at 13 frames min^{-1} and 15 frames min^{-1} respectively. All microfluidic experiments were conducted at 22°C . We imaged microfluidic experiments using a Zeiss Axio Observer inverted microscope with a Zeiss 20X Plan Apochromat objective, Zeiss AxioCam MRm camera, and a Zeiss Definite Focus system. Fluorescent cells were imaged using either a Zeiss LSM 700 scanning laser confocal system (Fig. 1G) or with a Zeiss HXP 120C light source (Fig. 1F, Fig. S1).

Experiments using Bioflux microfluidic devices

The test sections of all Bioflux channels were $350 \mu\text{m}$ wide and $75 \mu\text{m}$ deep, but they came in two slightly different designs (Fig. S2). Studies with fluorescein dye showed the different geometries of these designs upstream of the test section caused them to generate slightly different chemical distributions (Fig. S2A,D). We accounted for these differences in the model of diffusion that simulates the distribution of chemoattractant in these devices (see Fig. S2B,C,E,F, and section below).

The experiments in Fig. 2 were conducted using the Bioflux “Invasion” channels (Fig. S2). To continuously track the location of the chemoattractant in these experiments, we mixed the solution containing DMSO or succinate with Chicago Sky Blue 6B dye (3% by volume of saturated stock solution, Sigma Aldrich). Both dye and cells were visualized simultaneously within the same image. We confirmed in a separate experiment that the dye did not induce a chemotactic response (Fig. S15). Every 3 hours we reversed the direction of the chemoattractant gradient by manually replacing the fluid in the reservoirs that were connected to each inlet. While this process took approximately five minutes, it required that the microfluidic system be removed from the microscope and thus it was not possible to continuously image cells as the chemoattractant gradient changed direction. Thus, to quantify reversals in cells responding to a change in the chemoattraction direction (Fig. 4D,E,F,G) required the development of a custom microfluidic device (Fig. S11) that did not have this limitation.

Alternating gradient experiment using custom microfluidic device

To observe cells as they respond to a chemoattractant gradient that alternates in direction, we designed a microfluidic device with four inlet ports (Fig. S11). Molds with this design were fabricated from SU-8 on a silicon wafer (FlowJEM, Toronto, Canada). Microfluidic channels were cast using PDMS (Sylgard 184, Dow Corning) and holes for tubing were punched using a Harris Unicore 1.5 mm biopsy tool (Agar Scientific). Cured PDMS was bonded to glass coverslips (50 mm by 75 mm, No. 1 thickness, Agar Scientific) with a corona treater (BD-20AC, Electro-Technic Products) using previously described techniques (5). Tygon microbore tubing (0.06

inch outside diameter) was used to plumb both the inlets and outlets of the device. The outlet was connected to a single 10 ml syringe (Becton Dickinson) mounted on a syringe pump (PhD Ultra, Harvard Apparatus) that generated flow through the device via suction. The test section of the device is 600 μm wide and 75 μm deep.

After the system was primed with TB, exponential phase cells (WT or $\Delta pilG$) were drawn into the device at 100 $\mu\text{l min}^{-1}$ using the pair of inlets marked “A” in Fig. S11. After cells reached the test section, tubes connected to all four inlets were clamped with hemostats for 20 mins to allow cells to attach to surfaces in the absence of flow. Next, the tubing connected to the inlets were inserted to reservoirs containing either TB or 350 mM DMSO and Chicago Sky Blue 6B dye dissolved in TB. We then pulled fluid through the device at 100 $\mu\text{l min}^{-1}$ to both remove planktonic cells and allow the chemoattractant to reach test section of the device. The flow was then reduced to 5 $\mu\text{l min}^{-1}$ for the remainder of the experiment. We then clamped the tubes connected to one pair of inlets, which exposed cells to a DMSO gradient. Next, we changed the direction of the gradient approximately every eight minutes by sequentially unclamping and clamping the tubes connected to the inlets marked “A” and “B” in Fig. S11. Our analysis began at $t = 0$, when we first changed the direction of the gradient. Dye and cells were imaged simultaneously every four seconds at $x = 2.5$ mm (Fig. S11). While the distribution of dye was analyzed in each frame, cells were tracked in every other frame (i.e. every eight seconds) owing to computational constraints.

Preliminary experiments showed that the vast majority of correct reversals occurred within eight minutes of the gradient changing direction (Fig. 4G, white bars). Since the total duration of experiments is limited by cell crowding, we reversed the gradient

every eight minutes to generate as many reversals as possible before the surface became densely covered with cells and the tracking of individuals became difficult.

Characterization of concentration field in Bioflux devices using fluorescein and mathematical modeling

The distribution of chemoattractant, C , within the Bioflux devices was mapped using fluorescein, a fluorescent dye whose diffusion coefficient, D , approximates that of the low molecular weight compounds used in this study. Fluorescein was observed to strongly affect cell growth, so we conducted separate experiments without cells to resolve the distribution of C and mapped this back onto experiments with cells.

Imaging was conducted using the microscopy setup noted above except with a Zeiss EC Plan Neofluar 10X objective, a Zeiss LSM 700 scanning laser confocal unit to measure fluorescent intensity, and a Zeiss LSM T-PMT unit to simultaneously visualize the channel geometry. We recorded z -stacks of images at multiple, overlapping positions along the length of the device and the maximum fluorescent intensity in z was used to obtain the relative fluorescein concentration at each x,y position. Slight variations in C occurred along x because thermally induced fluctuations in z led to differences in the maximum measured fluorescent intensity between adjacent images (Fig. S2A,D).

To correlate cell movement with the chemoattractant distribution we used a mathematical model to calculate C within the Bioflux devices. More specifically, we used a one dimensional, time dependent diffusion equation to simulate molecular diffusion in the y direction and then used the mean flow velocity in the device to

transform time into distance along x . We consider a one-dimensional domain with impermeable, no-flux boundaries at $y = -L/2$ and $y = L/2$. At $t = 0$ two regions of constant concentration are initialized: $C = C_{MAX}$ in the region $-L/2 < y < h - L/2$ and $C = 0$ in the region $h - L/2 < y < L/2$. Subject to these initial and boundary conditions, the solution of the one dimensional diffusion equation is given by (6):

$$C = C_{MAX} \left\{ \frac{h}{L} + \frac{2}{\pi} \sum_{n=1}^{\infty} \frac{1}{n} \sin \frac{n\pi h}{L} \exp(-Dn^2\pi^2 t/L^2) \cos \frac{n\pi(y+L/2)}{L} \right\}.$$

This time dependent solution was transformed, assuming constant advection speed, to distance along the device via the substitution $t = x U^{-1}$, where $U = 42 \mu\text{m s}^{-1}$ is the mean flow velocity, $L = 350 \mu\text{m}$ is the channel width, and $D = 10^2 \mu\text{m}^2 \text{s}^{-1}$. This approach assumes uniform flow and that the distribution of chemoattractant is constant over the depth of the device. For modeling the Bioflux “Invasion” plates, which are symmetric about $y = 0$, we used $h = L/2 = 175 \mu\text{m}$, which yielded a distribution of C that closely matched that obtained experimentally using fluorescein dye (Fig. S2D,E,F).

For modelling the Bioflux “WPM” plates, which have a slight asymmetry upstream of the test section, we used $h = 160 \mu\text{m}$ and introduced an offset in y to directly match position of the $C = 0.5$ isocontour in the fluorescein experiment (Fig. S2A,B,C). This concentration field was used exclusively for presentation purposes (Fig. 1B), but not for any quantitative analyses.

Modeling the chemical environment in the alternating gradient experiment

In the alternating gradient experiment, we used a larger flow velocity

($U = 1.85 \text{ mm s}^{-1}$) to minimize the variation in chemical stimuli along the x direction of the device. The characteristic width of the gradient generated by diffusion can be approximated as $L \approx \sqrt{2Dx/U}$ and we imaged at $x = 2.5 \text{ mm}$ (Fig. S11), yielding $L \approx 20 - 50 \text{ }\mu\text{m}$ for $D = 10^2 - 10^3 \text{ }\mu\text{m}^2 \text{ s}^{-1}$, which is in the range experimentally observed with the dye (Fig. 4D). Our field of view spans 0.45 mm in the x dimension: the formula above predicts that the width of the gradient increases by $\approx 10\%$ from the upstream to the downstream edge of our field of view. Thus, within our field of view, cells at the same y position experience nearly the same chemical environment regardless of their position in x . This small amount of variation allows us to average C along x to present its spatiotemporal variation as a kymograph (Fig. 4D,E) and pool cell behaviour along x (Fig. 4F,G).

Cell tracking

All images were processed using the open source software Fiji (3) and its associated plugins. After correcting the time series of images for thermally-induced drift of the microscope stage (using the Image Stabilizer plug in) and enhancing the contrast of cells (using background subtraction and noise reduction functions), we tracked the movement of cells through space and time using the TrackMate plug in (7). To distinguish solitary cells from those residing within groups, we calculated the mean image intensity within a $3 \text{ }\mu\text{m}$ radius from the centroid each detected cell. Cells in close proximity to other cells (e.g. those within a cluster) yielded larger mean intensities than solitary cells, which allowed us to exclude the former prior to running the tracking algorithm. To quantify cell length and cell orientation we fitted each cell with an ellipse at every time point, functionality that is accessible by running

Trackmate via a Jython script (this feature is not available in the Graphical User Interface). All tracking data was exported from Fiji to Matlab (Mathworks) for subsequent analysis.

Experiments where dye gradients and cells were visualized simultaneously within the same image (Figs. 2, 4D-G, and Figs. S12, S13, S14, S15) required additional processing. To isolate cells, we removed the variable intensity background by normalizing the local contrast with Fiji's Integral Image Filter plugin. To isolate the dye, we removed cells from the image using Fiji's Rolling Ball Background Subtraction function.

Analysis of cell behavior

Calculation of chemotactic bias

The strength of the chemotactic response, β , was quantified by dividing number of cells moving up the gradient by the number of cells moving down the gradient as a function of time. While analogous metrics have been used to quantify chemotaxis in swimming bacteria (8), twitching cells exhibit jerky, unsteady movement (9), such that the instantaneous direction of a cell's movement is not representative of the direction of its transport over longer timescales. Thus, in our calculation of β we defined the direction of movement using a cell's net displacement over the length of its trajectory (with the exception of Fig. 2, see below). In addition, we excluded non-motile cells and cells that do not exhibit appreciable movement from their origin. This was accomplished by calculating the net to gross displacement ratio (NGDR), which is defined as the straight line distance between the start and end points of a trajectory

divided by the total distance travelled along the path of the trajectory (10).

Trajectories with $\text{NGDR} < 0.15$ were excluded from our calculation. This threshold was chosen based on visual inspection to exclude cells with convoluted paths that do not show significant movement in any direction (trajectories with $\text{NGDR} < 0.15$ are shown in Movie S1). All measurements of β were obtained by analyzing cells within in two adjacent fields view of the microscope (with the exception of Fig. 2, see below), which spanned the full channel width in y and approximately from $x = -0.05$ to 0.85 mm.

The rose plots in Fig. 1B,C were obtained by calculating the angle, θ , from each trajectory's from origin to its terminus. The resulting angles were weighted by the trajectory length, binned within 12 equally spaced bins around the unit circle, and normalized to obtain the probability density function. As cell crowding significantly restricted cell movement at later time points, this analysis considered only trajectories collected from $t = 0$ to 5 h.

In Fig. 2, we quantified how cells react to changes in the direction of the gradient. To capture changes in motility that occur mid-trajectory, we subdivided trajectories into segments 16 minutes long and used these to calculate $\bar{\theta}$ (Fig. 2G) and β (Fig. 2H). This segment length is long enough to capture the overall direction of cell movement (smoothing over the frequent, rapid changes in movement direction that are characteristic of twitching motility), whilst being short enough capture the response of cells to the changing gradient with reasonable temporal resolution (Fig. 2G). The normalized gradient, G , at each point along the trajectory was calculated via bilinear interpolation from the mathematical model of diffusion (Fig. S2F) and was averaged to obtain the mean G for each segment. In these experiments cells were imaged in

only one field of view, which spanned the full channel width in z and approximately from $x = -0.05$ to 0.43 mm.

Calculation of the apparent aspect ratio

To quantify the orientation of cells relative to the surface, we calculated cell length divided by the cell width to obtain its aspect ratio as viewed from below the surface (within an approximately $1\ \mu\text{m}$ depth of field along z). *P. aeruginosa* cells have an elongated cylindrical shape, such that when cells are oriented perpendicular to the surface they have an apparent aspect ratio of one, whereas cells oriented parallel to the surface yield an aspect ratio greater than one. The apparent aspect ratio of each cell was calculated over time and data from all trajectories were pooled to obtain the probability density function for each strain (Figs. S5B, S8).

Calculation of root mean squared displacement

The root mean square displacement (RMSD) measures how far cells venture from their initial position as a function of time, allowing us to objectively compare motility of between different strains (Fig. 3C) and in different chemical environments (Fig. S4). The RMSD is given by

$$\text{RMSD}(\tau) = \sqrt{\langle (x(\tau) - x_0)^2 + (y(\tau) - y_0)^2 \rangle},$$

where τ is the time lag, $[x_0, y_0]$ is a cell's initial position, and angled brackets denote averaging. When plotted on a log-log plot (Fig. S4B), the $\text{RMSD}(\tau)$ of twitching cells exhibits a slope of approximately one for small τ , denoting ballistic motion, and

transitions into a slope of approximately $\frac{1}{2}$ for larger τ , which corresponds to diffusive motion. Similar observations have been made for the motility of a diverse range of microorganisms (11).

Reversal detection

While the reversals in *M. xanthus* have been comprehensively studied (12), reversals in twitching *P. aeruginosa* have largely escaped mention in the literature (see Semmler et al 1999 (2) for an exception). One possible reason for this is that the latter occur much more infrequently: while *M. xanthus* cells reverse once every several minutes (13, 14), we find that on average *P. aeruginosa* cells reverse once every few hours (Fig. 4C). Reversals in *M. xanthus* are typically enumerated manually by direct observation (13, 14), but quantifying the relatively infrequent reversals exhibited by *P. aeruginosa* necessitated the development of an automated algorithm to detect reversal events among a large number of cell trajectories.

Cells tend to move along their long axis (Fig. S9) because they pull themselves along using pili that extend from their poles (15, 16). A reversal occurs when a cell stops and moves back in the other direction without turning. Under idealized conditions then a reversal occurs when a cell's body orientation, ϕ , remains constant, but its movement direction, θ , changes by $\pm\pi$ such that the leading pole becomes its trailing pole (Fig. S9). However, in practice both the unsteady, jerky movement of twitching motility and cell division (Fig. 4A, B) can generate events that a basic algorithm would misdiagnose as a reversal. Since “true” reversals are readily observed by eye (Movies S3, S4, S5, S6), our approach was to develop an algorithm that agrees with what one would obtain by direct observation. To achieve this, we developed a system

of filters to discriminate true reversals from spurious events and adjusted parameters of these filters using direct observation as a benchmark. Importantly, we used exactly the same method to analyze each experiment, allowing us to objectively compare the reversal rate in different strains and in different chemical environments.

To detect reversals in the static gradients, we first smoothed trajectories using a 10 min moving average filter (Fig. 4A) to calculate the mean movement direction, θ_M . At each time point along the trajectory we identify the leading pole by determining which of the cell's two poles is most closely aligned with the direction of cell movement (i.e. we determine whether ϕ or $\phi+\pi$ forms the smallest angle with θ_M). A potential reversal occurs when a cell's leading pole shifts to the opposite side of the cell between subsequent time points.

We used the same procedure to identify potential reversals in the alternating gradient experiments, but because reversals were induced more frequently and cells were tracked at a higher temporal resolution (every 8 seconds, as opposed to every minute in the static gradient experiments) we used a 160 second moving average filter to obtain θ_M .

After identifying potential reversals, we developed a series of filters to objectively resolve which of these are “true” reversals and which result from aberrant cell motion. Below we describe each of these filters and the specific cell behavior that they are designed to discriminate. Smoothed cell trajectories were used in each of these calculations.

We exclude potential reversals from:

1. Cells who are sliding sideways, for example, when they are pushed by flow. These cells have motility that is not aligned with the cell's long axis before and after the reversal. We measure the cosine of the angle between the direction of the leading pole and the direction of cell motility and reversals are excluded if this is smaller than 0.55.
2. Cells who are upright and only attached by one pole to the surface (whose mean apparent aspect ratio is smaller than 1.4 either before or after the reversal).
3. Cells who are non-motile (speed is smaller than $0.08 \mu\text{m min}^{-1}$ either before or after the reversal).
4. Cells who are rapidly pivoting about their point of attachment with the surface (whose bodies rotate more than $\pi/8$ radians between subsequent time points).
5. Cells that are jiggling back and forth on the surface. We do this by excluding cells that have experienced another potential reversal in the preceding or following 5 min in the static gradient experiments (2.4 min in the alternating gradient experiments).
6. Cells undergoing division. Cell division events were detected by measuring the change in cell length over time. We exclude potential reversals in trajectories that experience a large reduction in cell length immediately before or after a reversal. Apparent reversals arising from cell division are marked in Movies S3 and S4.

Calculation of reversal rate

To estimate the reversal rate, we divided the total number of reversals in an experiment by the cumulative time of all trajectories. In the calculation of the latter, we omitted the trajectories of weakly motile cells that are incapable of generating reversals (owing to our specification of a minimum cell speed, see previous section). This ensures consistency when comparing the reversal rate across experiments that may have different fractions of weakly motile cells.

In experiments with a static DMSO gradient (Fig. 4C) we separately measured the reversal rate of cells that are initially traveling down the gradient (white bars) and cells initially traveling up the gradient (black bars). The rate of “correct” reversals was calculated by dividing the total number of correct reversals by the cumulative time that trajectories moved down the gradient. Conversely, the rate of “incorrect” reversals was calculated by dividing the total number of incorrect reversals by the cumulative time that trajectories moved up the gradient. In both calculations, the cumulative time was adjusted using the cell speed consideration noted in the previous paragraph.

SI Figures

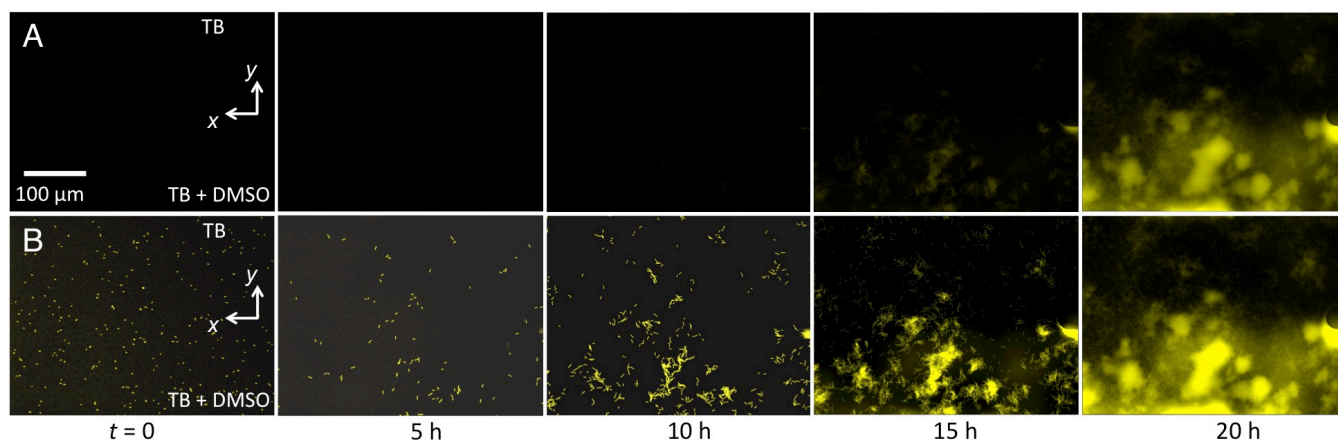


Figure S1: Quantifying the dynamics of biofilm formation using epifluorescent microscopy. (A, B) To illustrate how biofilms formed in our devices over time, we imaged cells that constitutively produce yellow fluorescent protein every two minutes to generate the kymograph shown in Fig. 1F. Shown here are five of the 600 epifluorescent images from this time series. Raw images are shown in (A), whilst each of the images shown in (B) has had the contrast adjusted such that the relatively weak signal from single cells is visible at early time points. At the beginning of the experiment cells are allowed to attach to the surface under quiescent conditions and then at $t = 0$ the flow used to generate the DMSO gradient is turned on (SI Materials and Methods). This flow detaches a fraction of the cells, so that there are fewer surface attached cells at $t = 5$ h. However, cell division leads to the formation of microcolonies by $t = 15$ h and by $t = 20$ h the biofilms are $\approx 20 \mu\text{m}$ thick (Fig. 1G).

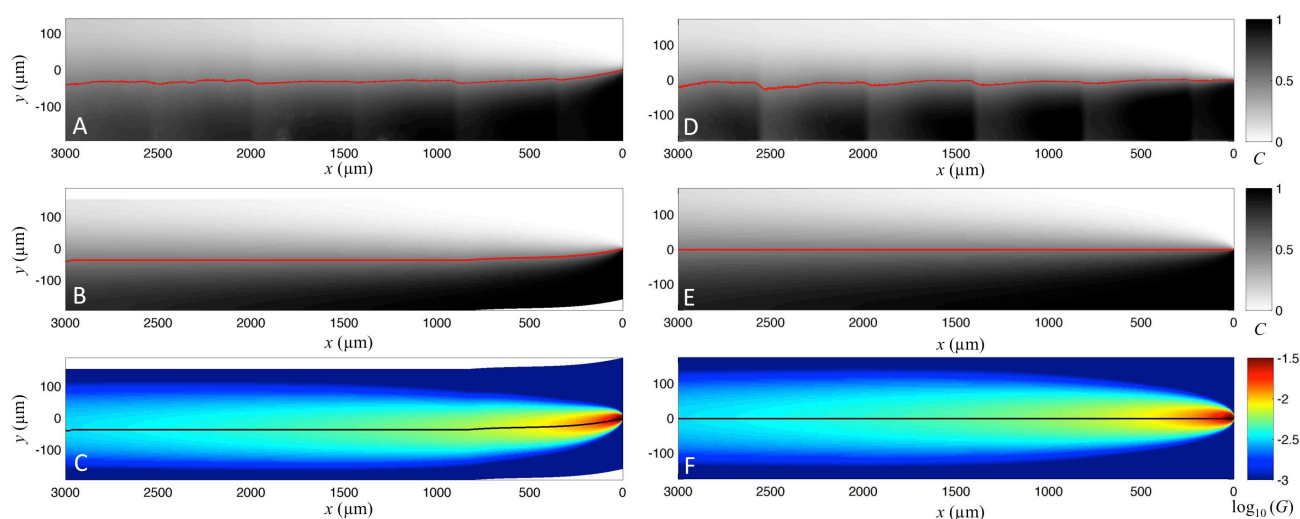


Fig. S2: A mathematical model accurately predicts the distribution of chemoattractant in two Bioflux microfluidic devices. The “WPM” channels (A, B, C) and “Invasion” channels (D, E, F) generate slightly different chemoattractant distributions owing to the different geometry of their inlets. In experiments without bacteria, we measured the normalized concentration, C , of fluorescein in each channel design using confocal microscopy (A, D, SI Materials and Methods). This distribution was simulated using an analytical model of molecular diffusion (B, E), which was then differentiated to obtain, G , the normalized chemoattractant gradient (C, F, Supplementary Methods). The $C = 0.5$ contour is marked with red line in the upper two rows and a black line in the lower row. The WPM channels generate a chemoattractant distribution slightly asymmetric about $y = 0$, which was accounted for in the model by matching the $C = 0.5$ contour from the empirical measurement (red line in A, SI Materials and Methods). Note the different scales in x and y .

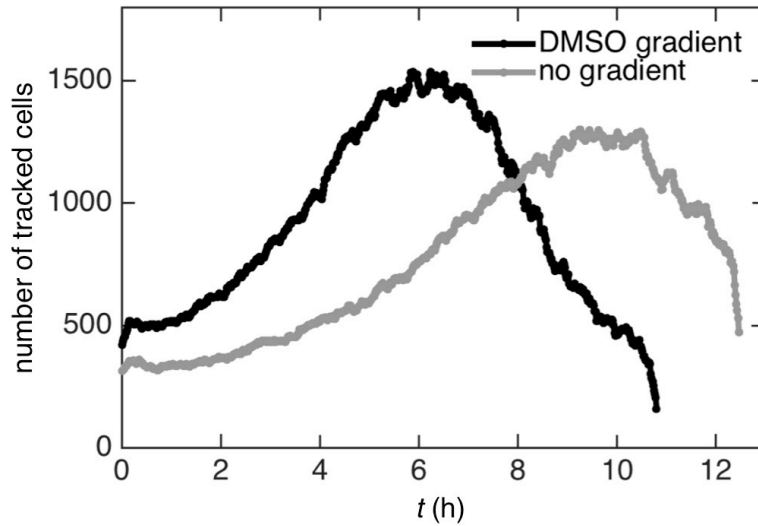


Fig. S3: Automated cell tracking allows us to measure the aggregate behaviour of a large number of cells. Here we plot the number of cells tracked within each frame of the experiments shown in Fig. 1. The number of cells initially increases as a result of cell division, but then decreases as cells crowd the surface such that individual cells can no longer be discerned (Movie S1). The analyses shown in Fig. 1D,E are derived from the trajectories of this large population of cells. The analyses shown elsewhere in this paper are derived from a similar number of cells.

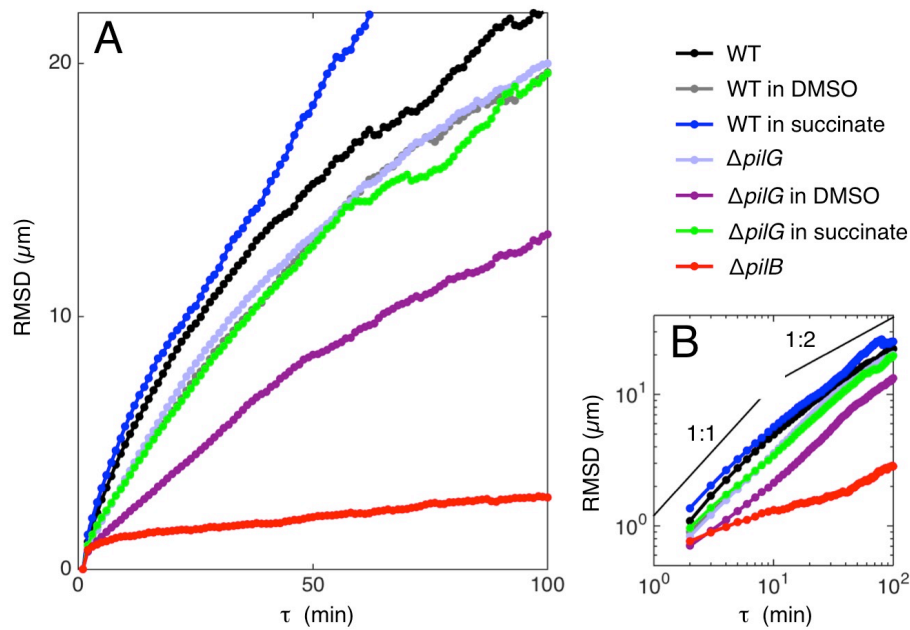


Fig. S4: Wild-type and $\Delta pilG$ cells exhibit reduced motility in the presence of DMSO, but not in the presence of succinate. Measurements of the root mean square displacement, RMSD, reveals that in DMSO cells venture a shorter distance from their origin over a time lag, τ . However, in succinate wild-type cells exhibit a larger RMSD than in the control, whilst the motility of $\Delta pilG$ cells is largely unaffected by succinate. Data for the nonmotile $\Delta pilB$ strain is shown for comparison. Here the RMSD is plotted as function of τ on linear (**A**) and logarithmic (**B**) axes. The line with a 1:1 slope in (B) corresponds to ballistic movement, whilst the 1:2 slope corresponds to diffusive movement. All experiments were performed in the absence of gradients in either pure TB, TB supplemented with 350 mM DMSO, or TB supplemented with 2 mM succinate.

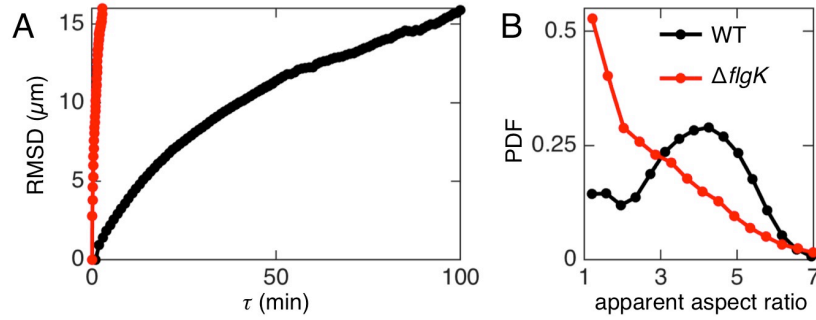


Fig. S5: Cells lacking flagella perform twitching motility and tend to stand upright on the surface. (A) The root mean squared displacement of $\Delta flgK$ cells is larger than that of wild-type cells at the same time lag τ , which means that flagellum-null cells move even faster than the wild-type. (B) $\Delta flgK$ cells tend to move with their long axis perpendicular to the surface such that their apparent aspect ratio (the cell length divided by cell width, as viewed from below the surface, SI Materials and Methods) is strongly peaked at unity, as we found for $\Delta pilH$ cells (Fig. S8). In comparison, wild-type cells typically orient themselves parallel to the surface such that their apparent aspect ratio peaks at ≈ 4 . These findings are in agreement with a previous study that also found cells lacking flagella have enhanced motility and increased propensity to stand upright (17).

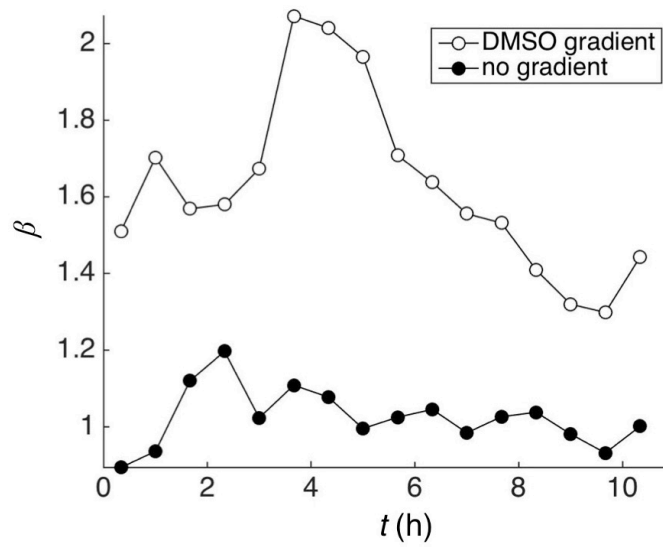


Fig. S6: The response regulator CheY1, which mediates chemotaxis in swimming *P. aeruginosa* cells (18-20), is not required for twitching chemotaxis. *cheY1*-null cells exposed to a gradient of DMSO (line with white circles) exhibit a chemotactic bias, β , much larger than they exhibit in the absence of chemical gradients (line with black circles), indicating that they are strongly chemotactic.

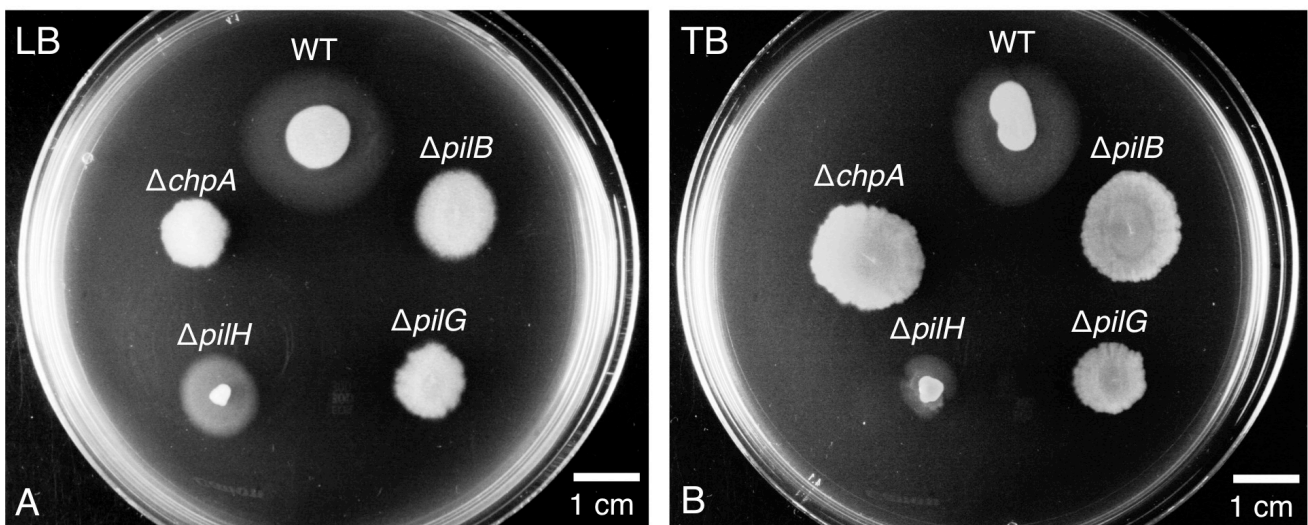


Fig. S7: The behaviour of Chp chemosensory mutants in agar-based “stab” assays. Twitching motility in this assay is detected by the formation of the so-called “twitching rings” (faint rings that form around colonies), which form at the bottom of plates, between the plastic and the agar. In-frame deletions of *pilB*, *chpA* and *pilG* prevent twitching rings while *pilH*-null cells form smaller twitching rings than the respective WT. We recapitulate the data published previously using plates containing Luria broth (LB, **A**) (1, 21) and also study twitching motility in plates containing tryptone broth (TB, **B**) as this is the growth medium used in our microfluidic experiments. Plates were imaged after 48 hours of incubation.

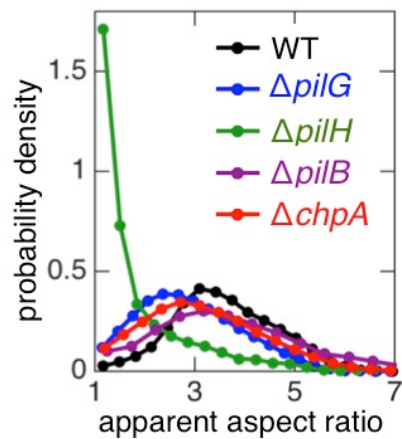


Fig. S8: Cells lacking PilH tend to move with their long axis perpendicular to the surface, leading to an apparent aspect ratio of ≈ 1 , whereas wild type cells and remainder of the Chp mutants we tested orient themselves parallel to the surface such that their apparent aspect ratio is >1 . Here the apparent aspect ratio is the cell length divided by cell width, as viewed from below the surface (SI Materials and Methods).

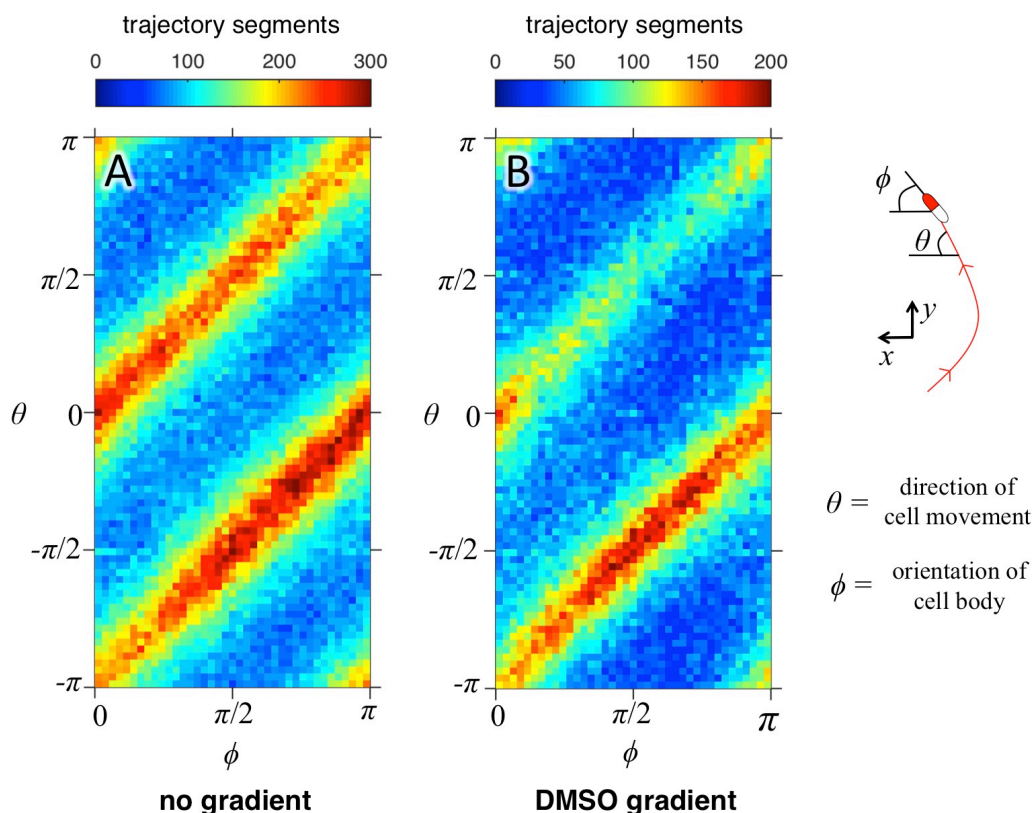


Fig. S9: Twitching cells tend to move along their long axis both the absence (A) and presence (B) of a DMSO gradient. The orientation of the cell body, ϕ , and the direction of cell motility, θ , were calculated at each time point along the trajectories (SI Materials and Methods). Each pair of angles was used to generate a histogram that shows their relative frequency in $\phi - \theta$ space. While the orientation of a cell body, which lacks polarity, can be fully specified by its angle in the half plane, $\phi = [0, \pi]$, cell motility can occur in any direction on the unit circle, $\theta = [-\pi, \pi]$. When a cell undergoes a “reversal”, ϕ remains constant, but θ shifts by $\pm\pi$. Strong clustering in (A) along the lines $\phi = \theta$ and $\phi = \theta - \pi$ reveals that in the absence of a gradient cells tend to move along their long axis, likely owing to fact that the pili, with which cells pull themselves along a surfaces, cluster at their poles (15, 16). A similar distribution is observed in a gradient of DMSO (B), but cells preferentially move along their long axis in the direction of increasing DMSO concentration.

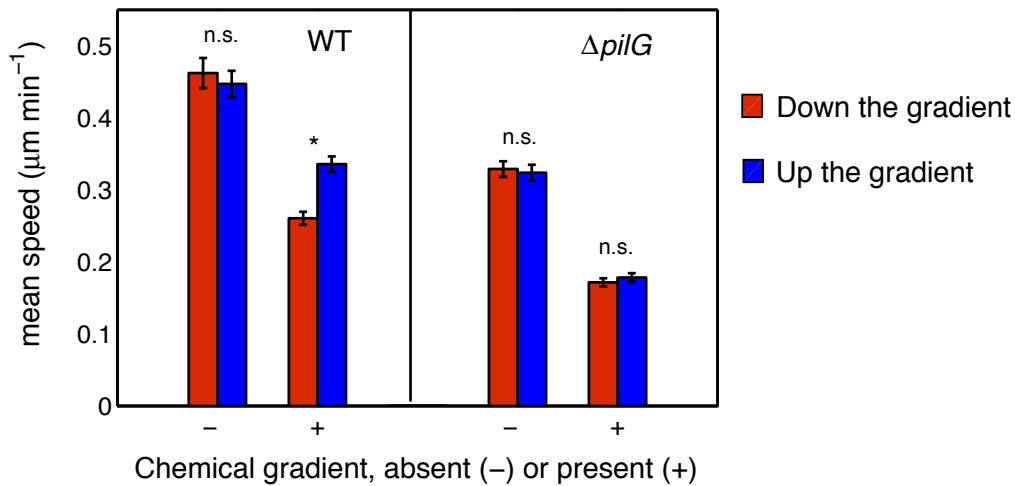


Fig. S10: Wild-type cells traveling towards the DMSO source (“up the gradient”) move approximately 25% faster than cells moving away from the DMSO source (“down the gradient”), but this asymmetry in speed is absent in *ΔpilG* cells and in gradient-free controls. (+) denotes data from experiments with a DMSO gradient, whereas (–) denotes data from control experiments which use pure tryptone broth (TB). For each experiment, we smoothed trajectories with a 10 min moving average filter and calculated the speed and direction of cell movement at each point along these smoothed trajectories. The resultant measurements of cell speed were pooled by whether they were recorded as the cell moved in the $-y$ or $+y$ direction, which correlates to “Up the gradient” and “Down the gradient” respectively. In the gradient-free controls, “Up the gradient” and “Down the gradient” correspond to cell speed in the same y direction as experiments with a DMSO gradient (Fig. 1). “n.s.” denote non-significant differences in speed while “*” denote a p -value < 0.05 , according to Wilcoxon rank tests at a significance of 5%. Error bars are standard errors of means. We note that the overall reduction in cell speed observed in experiments with DMSO is consistent with the observation that DMSO tends to reduce cell motility (Fig. S4).

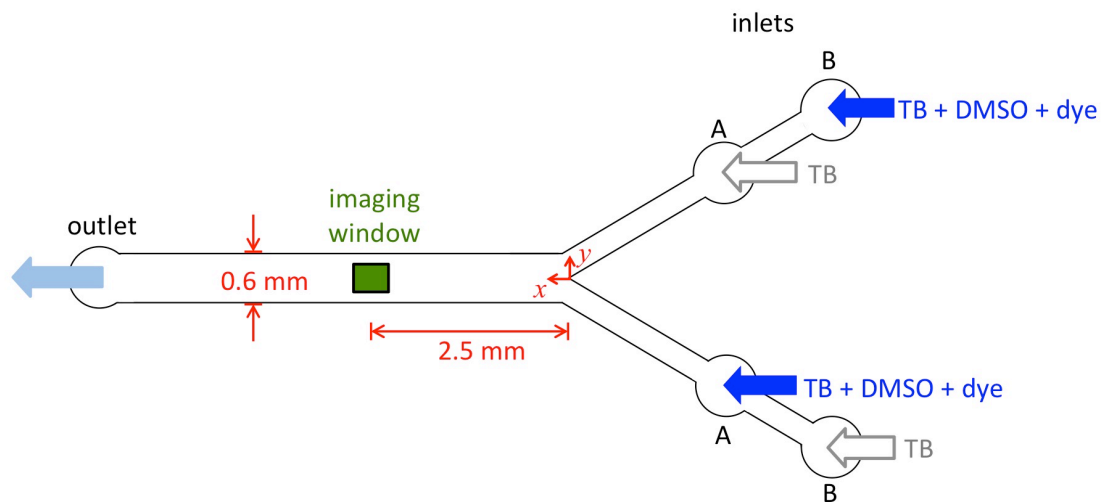


Fig. S11: A schematic of the custom microfluidic device used to rapidly alternate the direction of a chemoattractant gradient. The four inlets of the device were connected to reservoirs containing either TB mixed with DMSO and Chicago Blue dye or pure TB. Fluid was continuously withdrawn from the outlet and the pairs of inlets marked “A” and “B” were sequentially clamped (SI Materials and Methods) such that fluid is pulled from only one pair of inlets at a time. Moving the clamps to the opposite pair changes the direction of the chemoattractant gradient in the imaging window (green box). The channel is 75 μm deep.

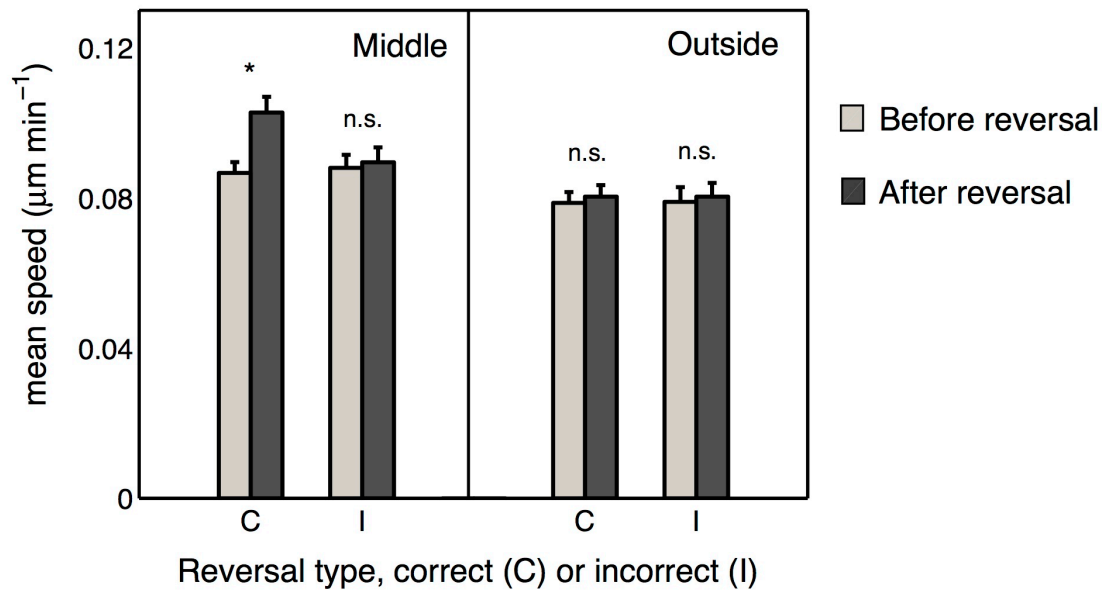


Fig. S12: Cells move faster after responding to a change in the direction of a chemoattractant gradient. We calculated the mean speed of individual cells before (light grey bars) and after (dark grey bars) they performed reversals (SI Materials and Methods), and pooled these according to whether they occurred in the “Middle” of the device (the region between the dashed lines in Fig. 4D,E), where spatial gradients are strongest, or on the “Outside” edges of the device (the region outside the dashed lines in Fig. 4D,E), where spatial gradients were relatively weak. Correct reversals occur in cells initially moving away from a chemoattractant source, and incorrect reversals occur in cells initially moving towards a chemoattractant source. Cells increase their speed after performing correct reversals in the middle of the channel, where they are induced at a higher rate (Fig. 4F). This asymmetry was not observed in the outside region or for incorrect reversals. “n.s.” denote non-significant differences in speed while “*” denotes a p -value < 0.05 , according to paired-sample t -tests at a significance of 5%. Error bars are standard errors of means.

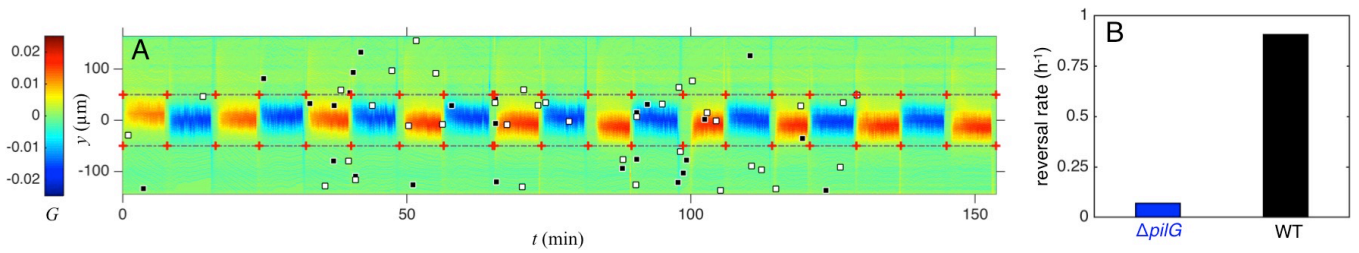


Fig. S13: Cells lacking the response regulator PilG cells rarely reverse direction in the alternating gradient experiment. (A) When $\Delta pilG$ cells were exposed chemoattractant conditions analogous to that shown in Fig. 4D, reversals (black and white boxes) occurred relatively infrequently when compared to the wild-type, which is consistent with the behavior of swimming $\Delta cheY1$ cells that rarely reverse their swimming direction and lack the ability to perform flagella-based chemotaxis (19). Data in A are presented in the same manner as Fig. 4D of the main text. (B) The reversal rate of $\Delta pilG$ and wild-type cells in the alternating gradient was quantified by dividing the total number of reversals (correct and incorrect) by the total time of trajectories (SI Materials and Methods), revealing that reversals occurred ≈ 13 times more frequently in the wild-type than in $\Delta pilG$.

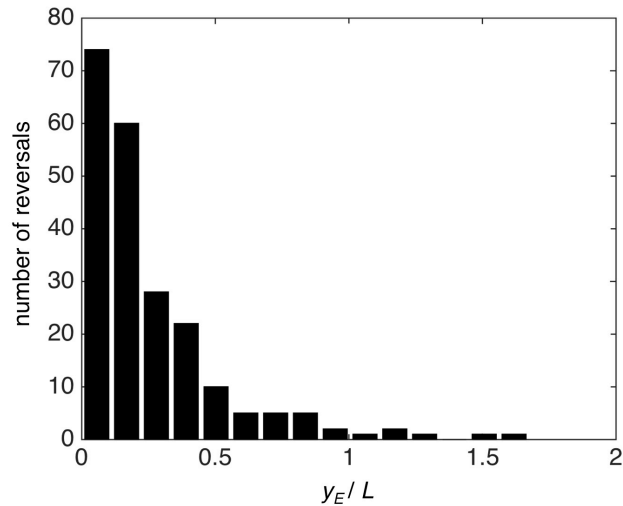


Fig. S14: Cells exposed to DMSO gradient that alternates direction respond quickly, typically reversing before they move a small fraction of their body length. Here we replot the data shown in Fig. 4G (inset), normalizing by the length of the cell body. After the gradient has changed direction, cells in our experiment move a distance, y_E , along the chemical gradient before they reverse to travel in the opposite direction. If cells sensed chemical gradients temporally, like swimming cells do (22), they would be able to measure the change in concentration over this distance. However, if cells measured gradients with a spatial mechanism, they would be able to measure the change in concentration over the entire length of their bodies, L . Thus, after the gradient has changed direction, a cell sensing in time would measure a change in concentration y_E / L smaller than a cell sensing in space. As in Fig. 4G (inset), the data shown here is for correct reversals in the middle of the device. Here y_E and L are the projections of cell movement and body length, respectively, along the gradient (i.e. in the y direction).

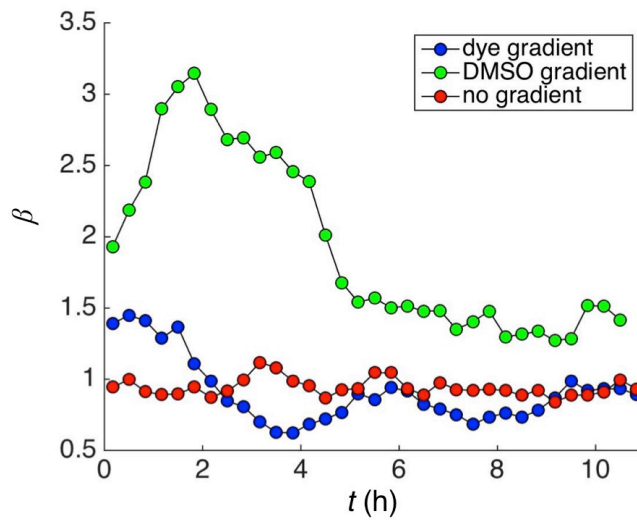


Fig. S15: Cells do not exhibit appreciable chemotaxis to Chicago Blue dye. The chemotactic bias, β , of cells in a gradient of dye (blue line) lacks the strong response observed in a gradient of DMSO (green line) and more closely resembles that of a gradient-free control (red line). We used this dye in alternating gradient experiments to track the distribution of chemoattractant within the microfluidic device.

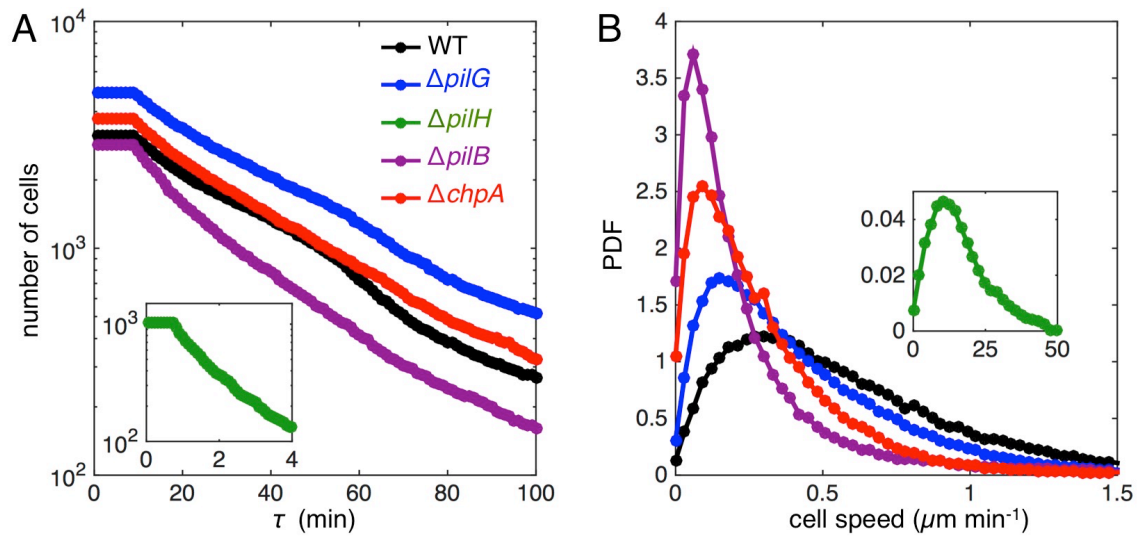


Figure S16: Quantification of the motility of Chp mutants. (A) In Fig. 3C we measure the root mean square displacement (RMSD) of cells in the absence of a chemical gradient to resolve the motility of different mutants of the Chp system. Here we show the number of cells from which these measurements were obtained. At small time lags, τ , RMSD is calculated from more than 1000 cells; whilst at the longest time lags are data is derived from more than 100 cell trajectories. To reduce the potential for spurious cell trajectories, we omit trajectories shorter than ten frames long from our analyses, which is responsible for the plateau observed at small τ . (B) The probability density function (PDF) of instantaneous cell speed shows the same trends as measurements of the RMSD (Fig. 3C). In both A and B, data for $\Delta pilH$ is shown in the insets. The axes of the insets are the same as the larger panel.

SI References

1. Bertrand JJ, West JT, & Engel JN (2010) Genetic analysis of the regulation of Type IV pilus function by the Chp chemosensory system of *Pseudomonas aeruginosa*. *J Bacteriol* 192(4):994-1010.
2. Semmler ABT, Whitchurch CB, & Mattick JS (1999) A re-examination of twitching motility in *Pseudomonas aeruginosa*. *Microbiol-SGM* 145:2863-2873.
3. Schindelin J, *et al.* (2012) Fiji: an open-source platform for biological-image analysis. *Nat Methods* 9(7):676-682.
4. Benoit MR, Conant CG, Ionescu-Zanetti C, Schwartz M, & Matin A (2010) New device for high-throughput viability screening of flow biofilms. *Appl Environ Microb* 76(13):4136-4142.
5. Haubert K, Drier T, & Beebe D (2006) PDMS bonding by means of a portable, low-cost corona system. *Lab Chip* 6(12):1548-1549.
6. Crank J (1975) *The mathematics of diffusion* (Clarendon Press, Oxford) 2nd Ed pp viii, 414 p.
7. Jaqaman K, *et al.* (2008) Robust single-particle tracking in live-cell time-lapse sequences. *Nat Methods* 5(8):695-702.
8. Ahmed T & Stocker R (2008) Experimental verification of the behavioral foundation of bacterial transport parameters using microfluidics. *Biophys J* 95(9):4481-4493.
9. Jin F, Conrad JC, Gibiansky ML, & Wong GCL (2011) Bacteria use type-IV pili to slingshot on surfaces. *Proc. Natl. Acad. Sci. U.S.A.* 108(31):12617-12622.
10. Seymour JR, Marcos, & Stocker R (2009) Resource patch formation and exploitation throughout the marine microbial food web. *Am Nat* 173(1):E15-E29.
11. Visser AW & Kiorboe T (2006) Plankton motility patterns and encounter rates. *Oecologia* 148(3):538-546.
12. Zhang Y, Ducret A, Shaevitz J, & Mignot T (2012) From individual cell motility to collective behaviors: insights from a prokaryote, *Myxococcus xanthus*. *FEMS Microbiol Rev* 36(1):149-164.
13. Kearns DB & Shimkets LJ (1998) Chemotaxis in a gliding bacterium. *Proc. Natl. Acad. Sci. U.S.A.* 95(20):11957-11962.
14. Shi WY, Ngok FK, & Zusman DR (1996) Cell density regulates cellular reversal frequency in *Myxococcus xanthus*. *Proc. Natl. Acad. Sci. U.S.A.* 93(9):4142-4146.
15. Cowles KN & Gitai Z (2010) Surface association and the MreB cytoskeleton regulate pilus production, localization and function in *Pseudomonas aeruginosa*. *Mol Microbiol* 76(6):1411-1426.
16. Skerker JM & Berg HC (2001) Direct observation of extension and retraction of type IV pili. *Proc. Natl. Acad. Sci. U.S.A.* 98(12):6901-6904.
17. Conrad JC, *et al.* (2011) Flagella and pili-mediated near-surface single-cell motility mechanisms in *P. aeruginosa*. *Biophys J* 100(7):1608-1616.
18. Kato J, Kim HE, Takiguchi N, Kuroda A, & Ohtake H (2008) *Pseudomonas aeruginosa* as a model microorganism for investigation of chemotactic behaviors in ecosystem. *J Biosci Bioeng* 106(1):1-7.
19. Masduki A, *et al.* (1995) Isolation and characterization of chemotaxis mutants and genes of *Pseudomonas aeruginosa*. *J Bacteriol* 177(4):948-952.
20. Sampedro I, Parales RE, Krell T, & Hill JE (2014) *Pseudomonas* chemotaxis. *FEMS Microbiol Rev* 39(1):17-46.
21. Fulcher NB, Holliday PM, Klem E, Cann MJ, & Wolfgang MC (2010) The *Pseudomonas aeruginosa* Chp chemosensory system regulates intracellular cAMP levels by modulating adenylate cyclase activity. *Mol Microbiol* 76(4):889-904.
22. Berg HC (2004) *E. coli in motion* (Springer, New York).